

## Structure of Florida Thunderstorms Using High-Altitude Aircraft Radiometer and Radar Observations

G. M. HEYMSFIELD,\* I. J. CAYLOR,<sup>†</sup> J. M. SHEPHERD,\* W. S. OLSON,\*\*  
S. W. BIDWELL,\* W. C. BONCYK,\* AND S. AMEEN<sup>†</sup>

\*NASA/Goddard Space Flight Center, Greenbelt, Maryland; <sup>†</sup>Science Systems and Applications, Inc.,  
Lanham, Maryland; \*\*Caelum Research Corp., Silver Spring, Maryland

(Manuscript received 16 March 1995, in final form 20 February 1996)

### ABSTRACT

This paper presents an analysis of a unique radar and radiometer dataset from the National Aeronautics and Space Administration (NASA) ER-2 high-altitude aircraft overflying Florida thunderstorms on 5 October 1993 during the Convection and Moisture Experiment (CAMEX). The observations represent the first ER-2 Doppler radar (EDOP) measurements and perhaps the most comprehensive multispectral precipitation measurements collected from a single aircraft. The objectives of this paper are to 1) examine the relation of the vertical radar reflectivity structure to the radiometric responses over a wide range of remote sensing frequencies, 2) examine the limitations of rain estimation schemes over land and ocean backgrounds based on the observed vertical reflectivity structures and brightness temperatures, and 3) assess the usefulness of scattering-based microwave frequencies (86 GHz and above) to provide information on vertical structure in the ice region. Analysis focused on two types of convection: a small group of thunderstorms over the Florida Straits and sea-breeze-initiated convection along the Florida Atlantic coast.

Various radiometric datasets are synthesized including visible, infrared (IR), and microwave (10–220 GHz). The rain cores observed over an ocean background by EDOP, compared quite well with elevated brightness temperatures from the Advanced Microwave Precipitation Radiometer (AMPR) 10.7-GHz channel. However, at higher microwave frequencies, which are ice-scattering based, storm evolution and vertical wind shear were found to be important in interpretation of the radiometric observations. As found in previous studies, the ice-scattering region was displaced significantly downshear of the convective and surface rainfall regions due to upper-level wind advection. The ice region above the rain layer was more opaque in the IR, although the 150- and 220-GHz brightness temperatures  $T_b$  approached the IR measurements and both corresponded well with the radar-detected ice regions. It was found that ice layer reflectivities and thicknesses were approximately 15 dBZ and a few kilometers, respectively, for detectable ice scattering to be present at these higher microwave frequencies.

The EDOP-derived rainfall rates and the simultaneous microwave  $T_b$ 's were compared with single-frequency forward radiative transfer calculations using a family of vertical cloud and precipitation water profiles derived from a three-dimensional cloud model. Over water backgrounds, the lower-frequency emission-based theoretical curves agreed in a rough sense with the observed radar rainfall rate– $T_b$  data points, in view of the uncertainties in the measurements and the scatter of the cloud model profiles.

The characteristics of the ice regions of the thunderstorms were examined using brightness temperature differences  $\Delta T_b$  such as  $T_b(37 \text{ GHz}) - T_b(220 \text{ GHz})$ . The  $\Delta T_b$ 's (150–220, 89–220, and 37–86 GHz) suggested a possible classification of the clouds and precipitation according to convective cores, elevated ice layers, and rain without significant ice above the melting layer. Although some qualitative classification of the ice is possible, the quantitative connection with ice path was difficult to obtain from the present observations.

### 1. Introduction

Rainfall and latent heat release are important components of the earth's hydrological cycle, and they play a major role in driving the upward branches of the Hadley and Walker circulations in the Tropics. Consequently, there has been intense interest in measuring rainfall globally from space. Spaceborne rain measure-

ments have had a long history including use of passive microwave (e.g., Wilheit et al. 1977; Spencer 1986; Simpson et al. 1988) and infrared (IR) approaches (Adler and Negri 1988). Passive microwave-based precipitation algorithms have been greatly advanced since 1987 with the launch of the Defense Meteorological Satellite Program (DMSP) polar-orbiting satellite series, which include the Special Sensor Microwave/Imager (SSM/I) with frequencies from 19 to 86 GHz. Microwave-based algorithms have been developed ranging from simple (Adler et al. 1993) to more sophisticated microwave rain retrievals (Kummerow et al. 1989; Smith et al. 1994; Olson 1989). These retriev-

---

Corresponding author address: Dr. Gerald Heymsfield, NASA/GSFC, Code 912, Greenbelt, MD 20771.  
E-mail: heymsfie@carmen.gsfc.nasa.gov

als use the different scattering and emission characteristics of microwaves at frequencies from 6.6 to 86 GHz to retrieve rainfall rate and vertical precipitation structure. The first satellite mission dedicated to measure tropical and subtropical rainfall using passive microwave, IR, and radar remote sensors is the Tropical Rain Measuring Mission (TRMM) to be launched in 1997. TRMM is focused on global monthly rain estimates over  $5^\circ \times 5^\circ$  regions with measurement accuracies to within 10%, and vertical rain structure to be used in estimating latent heating profiles. While satellite rain estimation has focused on the global scale, the importance of precipitation measurements on smaller scales ranging from the mesoscale down to the convective scale has been recognized. The individual convective cloud elements with space and timescales less than 10 km and a few hours, respectively, provide the building blocks of mesoscale systems, which can be composed of convective and stratiform precipitation regions (Houze 1977).

Observational and theoretical understanding of spaceborne remote sensing of precipitation can be improved using aircraft instrumented with high-resolution radiometers and radars. Measuring precipitation from space requires a comprehensive set of algorithms that relate passive microwave, IR, and radar measurements to rainfall (Simpson 1988). Satellite radiometric measurements are inherently difficult to interpret in terms of vertical structure. Presently there are no spaceborne precipitation radars, and thus "ground truth" using aircraft or ground-based radars along with aircraft radiometric measurements is essential for validating future spaceborne radar and radiometer algorithms. Previous aircraft campaigns have provided an important means to validate passive microwave and visible-IR radiometric measurements from the National Aeronautics and Space Administration (NASA) ER-2 aircraft (Heymsfield and Fulton 1988; Spencer et al. 1989; Adler et al. 1990; Vivekanandan et al. 1989; Smith et al. 1994) and radar and passive microwave measurements from the DC-8 aircraft (Wang et al. 1994; Durden et al. 1994). The aircraft have provided high-resolution measurements of convection, which have improved the understanding of cloud microphysics (Fulton and Heymsfield 1991; Vivekanandan et al. 1993).

The ER-2 carries a comprehensive payload of passive and active instruments that provide information on microphysical and radiative properties of clouds (Kakar 1993). The passive instruments cover a wide range of frequencies from the visible to high-frequency microwave. The ER-2, which flies higher than the DC-8 (20 km vs 12 km), provides higher-frequency microwave measurements and cross-track scanned radiometric measurements from all channels compared to fixed nadir and off-nadir measurements for the DC-8. Aircraft measurements using the ER-2 have provided insight into the interpretation of top-of-atmosphere (TOA) microwave and IR brightness temperatures at

frequencies ranging from 18 to 183 GHz (Hakkarinen and Adler 1988; Heymsfield and Fulton 1988; Spencer et al. 1989; Adler et al. 1990; Vivekanandan et al. 1993). These studies have shown the dominance of ice scattering at the higher microwave frequencies and emission/absorption processes at lower frequencies.

In previous studies, the ER-2 observations have provided valuable information on convective events with small time and space scales and the structure of rain when used jointly with ground-based Doppler and multiparameter radars (e.g., Fulton and Heymsfield 1991; Vivekanandan et al. 1993). These comparisons with ground-based radars are, however, limited by difficulties in coregistering the airborne and ground-based datasets. Often in tropical convective events, a few minutes time and/or a few kilometers location error can produce significant differences in the inferred vertical precipitation structure. Therefore, it is desirable to have simultaneous aircraft radar and radiometer measurements to reduce uncertainties in the registration of the datasets. Aircraft datasets that have simultaneous and coincident radar and radiometer data are scarce, and only recently have joint radar and passive microwave measurements been available using the NASA DC-8 aircraft (Wang et al. 1994). Wang et al. recently reported 10-GHz radar and 10–92-GHz radiometer observations from passes over Typhoon Flo in the North Pacific. They examined the relationship between measured brightness temperatures and radar estimated rainfall rate.

In oceanic regions, space-based measurements are the only means to measure mesoscale convective systems (MCS) on a routine basis, while over land regions, satellite measurements can augment conventional radar measurements, which provide detailed internal structure information. However, the spaceborne measurements with coarse resolution, measure MCS characteristics indirectly. Often the interpretations are dependent on understanding of the microphysical structure of clouds—that is, the distributions of hydrometeors both spatially and vertically. The importance of vertical profiles of hydrometeors on TOA microwave temperatures has been addressed using forward radiative transfer models (e.g., Adler et al. 1990) and the retrieval methods described earlier. The microwave emission and scattering processes are dependent on hydrometeor types, shapes, sizes, and their vertical distribution. Modeling efforts in general are limited by the lack of knowledge of various microphysical aspects such as ice particle characteristics (shapes, sizes, water coating, etc.). The microphysics depends in a complicated fashion on thermodynamical aspects, vertical motion fields, storm evolution, and electrification. Radiative transfer modeling of the ice phase region is particularly difficult to validate because of the lack of detailed microphysical information.

During September and October 1993, an experiment called the Convection and Atmospheric Moisture Ex-

periment (CAMEX) was conducted at the NASA Wallops Flight Facility (Griffin et al. 1994). This experiment was aimed at 1) measurements of temperature, water vapor, clouds, precipitation and electrical fields; 2) radiometric signatures at high incidence angles; and 3) providing validation for the Special Sensor Microwave/Temperature-2 (SSM/T2) moisture sounding DMSP instrument, which has channels covering the 183-GHz water vapor line. Part of the CAMEX objectives were to provide further opportunity to meet moisture sounding objectives not met during the Tropical Ocean Global Atmosphere Coupled Ocean-Atmosphere Response Experiment (TOGA COARE). The ER-2 was the principal instrument platform of the experiment and several ground-based lidar sounders were situated near Wallops. Along with microwave and visible/IR radiometers, the ER-2 Doppler radar (EDOP) was included in the experiment with the objective to perform extended engineering flights and to collect scientific data.

This paper presents an analysis of the first joint radar-radiometer dataset from the ER-2, which was collected on 5 October 1993 during CAMEX. EDOP took measurements on the 5 October 1993 flight to southern Florida, when convective and stratiform precipitation regions over ocean and land backgrounds were overflown. These ER-2 data will be presented along with the passive radiometer data and other supporting observations from the WSR-88D radars at Melbourne and Miami, Florida, and conventional upper-air and surface data. These data are perhaps the most complete radar and radiometer dataset collected from a single aircraft. At present, there are no satellites until the launch of TRMM which contain the diversity of instruments that are presently on the ER-2 aircraft. The objectives of this paper are to 1) examine the relation of the vertical radar reflectivity structure to the radiometric responses over a wide range of remote sensing frequencies, 2) examine the limitations of rain estimation schemes over land and ocean backgrounds based on the observed vertical structure observations and brightness temperatures, and 3) assess the usefulness of scattering-based microwave frequencies (86 GHz and above) to provide information on vertical structure in the ice region. The EDOP data provide crucial information on vertical hydrometeor structure—that is, the definition of the melting level, the convective core locations and heights, the relative amounts of ice aloft, rainfall rates, and the freezing level. The microwave radiometer data from convective regions, when analyzed in isolation, sometimes leads to confusing interpretations because of a lack of detailed knowledge of the ice and liquid microphysics. Section 2 includes a description of the remote sensing instrumentation flown during CAMEX. Section 3 provides a brief discussion of EDOP flight tracks on 5 October 1993 and the environmental conditions present during the data collection period. Section 4 presents the combined radar-radiometer observations

over ocean and land, and section 5 provides a discussion of the radar and radiometer observations and their implications for spaceborne precipitation measurements. Section 6 provides a discussion of the structure of the ice region using the higher-frequency microwave measurements.

## 2. ER-2 instrumentation during CAMEX

### a. Description of ER-2 instruments

Rain measurements with microwave radiometers fall into absorption/emission and scattering-based regimes (e.g., Wilheit 1986). Emission-based measurements are generally made below the 22-GHz water vapor line and are primarily applicable over ocean backgrounds. These low-frequency measurements represent observations of the liquid hydrometeors themselves, and the theory relating attenuation to rainfall is direct and can be based on first principles. The scattering-based measurements are generally taken above the 60-GHz oxygen band and can be used over land and ocean backgrounds. These measurements are based on ice scattering in upper portions of precipitation regions and represent an indirect measure of the rainfall near the surface. A high degree of correlation exists between low brightness temperatures in the 86-GHz SSM/I measurements and surface rainfall (Adler et al. 1993), since generally rain regions have associated ice regions aloft. These ice particles are sufficiently large to fall through the freezing level and turn to rain. The brightness temperatures observed at these higher frequencies depend in a complicated manner on details of the ice layer such as particle sizes, orientations, and shapes. In the intermediate frequency region between about 25 and 50 GHz, both scattering and emission approaches must be considered. Finally, infrared radiometric approaches infer rainfall indirectly by associating cloud top heights with rainfall amounts (e.g., Adler and Negri 1988).

The ER-2 payload consisted of sensors capable of measuring various aspects of the cloud and precipitation structure, moisture and temperature profiling, and cloud electrification. The specific instruments applicable to precipitation measurements consisted of the Advanced Microwave Precipitation Radiometer (AMPR) the Multispectral Atmospheric Mapping Sensor (MAMS), the Millimeter-Wave Imaging Radiometer (MIR) and EDOP. These instruments are described briefly as to their purpose and characteristics. The EDOP instrument will be described in the next subsection.

The AMPR instrument was developed primarily for investigation of the internal structure of rain systems with various applications in atmospheric and land processes (Vivekanandan et al. 1993; Spencer et al. 1994). AMPR is a total-power passive radiometer with channels at frequencies of 10.7, 19.35, 37.1, and 85.5 GHz.

The lower frequencies respond to emission from raindrops, while the higher frequencies respond primarily to scattering from ice particles. The instrument is located in the Q-bay (lower fuselage behind pilot) of the ER-2 and scans 50 points cross-track  $\pm 45^\circ$  at approximately 3 s intervals; the sampling pattern is such that measurements are obtained at 0.6-km intervals both cross- and along-track. The beamwidths of the AMPR are  $1.8^\circ$  at 85.5 GHz,  $4.2^\circ$  at 37.1 GHz, and  $8^\circ$  at 19.35 and 10.7 GHz, and the corresponding surface footprints range from approximately 0.6 km at 85.5 GHz to 2.8 km at 10.7 GHz. The instrument measures only a single polarization state from a dual-polarized feed horn. Since scanning is achieved by rotating a splash plate, the polarization state changes from fully horizontally polarized at  $-45^\circ$  on the left side of the ER-2 to fully vertically polarized at  $+45^\circ$  on the right side; the polarization state is  $45^\circ$  at nadir. During CAMEX, the EDOP backscattered signal produced some interference on the AMPR 10.7-GHz channel between approximately  $\pm 12^\circ$  in scan angle (the AMPR antenna main and side lobes convolved with the EDOP backscattered return). Checks on the data during the EDOP transmission period indicated the brightness temperatures were elevated by 0–15 K depending on the background radiometric signal; in rain regions typical bias values were less than 5 K. We have taken some caution in the subsequent quantitative use of the 10.7-GHz data.

The MIR is a total-power passive microwave radiometer with channels at frequencies of 89, 150,  $183.3 \pm 1$ ,  $183.3 \pm 3$ ,  $183.3 \pm 7$ , 220, and 325 GHz, and it is used for measurements of atmospheric water vapor and precipitation (Racette et al. 1996). For cloud and precipitation regions, the channels on this instrument respond primarily to scattering from ice regions of clouds, with the lower frequencies penetrating progressively farther into the cloud (e.g., Gasiewski 1992). The 183-GHz channels respond to water vapor absorption and will not be discussed in this paper. The 183-GHz and lower-frequency channels on MIR are currently flown on the SSM/I and SSM/T2 spaceborne instruments. The MIR instrument is located in the right ER-2 wing superpod and scans 57 points cross-track  $\pm 50^\circ$  (each scan cycle takes about 2.9 s). All channels have a beamwidth of approximately  $3.3^\circ$  resulting in a spot size of about 0.5 km at a 10-km altitude typical of the ice scattering region in thunderstorms. The polarization state of the measurements rotates with scan angle such that at nadir, the electric field is perpendicular to the direction of flight.

The MAMS has eight visible/near-IR channels to measure reflected radiation from the surface and clouds, and four IR channels to measure thermal emission from water vapor, clouds, and the surface. The instrument is a cross-track scanning ( $\pm 43^\circ$ ) radiometer with channels ranging from 0.485 to  $12.56 \mu\text{m}$  (Jedlovec et al. 1989). During CAMEX, its primary func-

tion was to measure water vapor using the  $6.5\text{-}\mu\text{m}$  channel. The MAMS data of interest in this paper are the  $0.63\text{-}\mu\text{m}$  visible and  $11.12\text{-}\mu\text{m}$  IR data, which are useful for providing cloud top structure and heights and insights on IR rain estimation schemes (e.g., Adler and Negri 1988). During CAMEX, MAMS was mounted in the rear of the right wing superpod on the ER-2. Its instantaneous resolution at the surface from 20-km altitude is approximately 100 m at nadir, which combined with a scan rate of 6.25 rps and 717 samples in a scan, provides oversampling with scan lines spaced at 32-m intervals along-track. The instrument had limited dynamic range because the data system provided only 8-bit digitization; thus for the window channel IR, two separate  $11.12\text{-}\mu\text{m}$  channels with different dynamic ranges suitable for background (warm) and cloud (cold) features were utilized (Jedlovec et al. 1989). The raw aircraft data were processed through a multi-step procedure to provide calibrated radiances and brightness temperatures (Gumley et al. 1994).

#### *b. EDOP instrument description and characteristics*

A new Doppler radar system (Heymsfield et al. 1993; Caylor et al. 1994) has been installed in the ER-2 to measure the vertical reflectivity structure and hydrometeor motions simultaneous with the radiometric measurements. EDOP is an X-band (9.72 GHz) Doppler radar located in the nose of the ER-2. The composite system generates a nadir oriented beam with a copolarized receiver and a  $30^\circ$  forward-directed beam with co- and cross-polarized receivers. The system characteristics are given in the appendix. The first EDOP flights during CAMEX focused on obtaining reflectivity measurements, with Doppler measurements planned for the next flight series. In this paper, only the nadir measurements are presented. The ER-2 on a particular mission generally flies straight flight lines for as long as a few hundred kilometers. EDOP thus maps out high-resolution time-height sections of nadir reflectivity in the CAMEX flights. The antennas have a  $3^\circ$  beamwidth and a spot size of about 1.2 km at the surface (assuming a 20-km aircraft altitude). EDOP has been designed as a turn-key system (i.e., no human intervention during flight) with real-time processing onboard the aircraft. During CAMEX, the system was configured for 150-m gate spacing and a pulse repetition frequency of 2200 Hz. On the 5 October flight, raw (unprocessed) reflectivity returns were recorded at a reduced rate (16 pulses per second rather than at the pulse repetition frequency of EDOP), and post-flight averaging was performed over 2-s intervals. Calibration of the EDOP data from CAMEX is described in Caylor et al. (1994). This post-processing has resulted in excellent vertical time–height images of reflectivity but with reduced sensitivity because of the reduced number of samples used in the averaging. Reflectivities have been thresholded to just above the noise level of

the averaged, nonrange corrected data. This resulted in minimum detectable reflectivities of approximately 10 dBZ at 10-km altitude and 16 dBZ at the surface; these values are more than 10-dBZ higher than present observations with the instrument but still are extremely useful for the present study.

### 3. Background of ER-2 flight on 5 October 1993

#### a. ER-2 flight tracks on 5 October 1993

The ER-2 objective on 5 October 1993 was to study convection in the south Florida region (Griffin et al. 1994). The aircraft took off from Wallops Island, Virginia, at 1600 UTC<sup>1</sup> for a 7-h flight. It flew along the east coast of the United States, reached the Florida peninsula at about 1800, and was then sent to a region of active thunderstorms south of Key West, arriving there at 1820. The segment of the ER-2 flight in the vicinity of southern Florida during which EDOP was operating is shown superimposed on radar images in Fig. 1. The ER-2 made two passes over a group of thunderstorms over the Straits of Florida during flight lines 2 (FL2) and 3 (FL3). (Hereafter FL $x$  denotes flight line  $x$ , as shown in Fig. 1.) As these thunderstorms dissipated, the ER-2 overflowed convection along the east coast of Florida (FL4a and FL4b). FL4a began as the ER-2 traversed Florida Bay and progressed northward inland along the Florida coast. FL4b was mostly over land, except at the very end of the flight line when the ER-2 progressed northeastward over the Atlantic Ocean. EDOP was switched off after 1920 to eliminate interference with the AMPR 10.7-GHz channel.

#### b. Meteorological conditions associated with ER-2 flight tracks

The synoptic-scale conditions on 5 October 1993 in the Florida region were a typical summer pattern with the 500-mb flow generally southerly as high pressure was building in the western Atlantic. A small upper-level low was located over the northwestern portion of the Gulf of Mexico. Visible satellite images from Geostationary Operational Environmental Satellite (GOES) at 1200 (not shown) indicated an area of thunderstorms south of Key West, which appeared to be associated with a weak baroclinic zone. Surface analyses indicated a prefrontal surface trough extending from just south of the keys northeastward on 4 October 1993 at 1200.

Clouds and precipitation over the peninsula on 5 October are primarily attributed to regional-scale forcing, which resulted in a fairly complex organization of sea and lake breeze convergence lines. A relatively unsta-

ble air mass was present at 1200 and surface dewpoints were already in the 23–26°C range. Surface winds were east-northeasterly over the entire peninsula. Soundings from Key West (EYW) in Fig. 2a and West Palm Beach (PBI) (not shown) indicated moderately unstable air with convective available potential energy (CAPE) values of 2309 and 1971 m<sup>2</sup> s<sup>-2</sup>, respectively. Bulk Richardson numbers (Ri) for the EYW and Palm Beach (PBI) soundings were 200 and 3200, respectively. These conditions are favorable for the development of multicell storms (Weisman and Klemp 1982). The EYW sounding is closest to the location of the thunderstorms observed during FL2 and FL3, while the PBI sounding is nearest thunderstorms observed during FL4a and FL4b. Further examination of the Key West sounding reveals an equilibrium level at about 13 km (158 mb), a 0°C level at about 4.7 km, and a lifting condensation level (LCL) representative of cloud base altitude of only 300 m. The winds were relatively strong (>15 m s<sup>-1</sup>) above 10 km (Fig. 2b).

The radar echoes in Fig. 1 depict the general evolution of thunderstorms from 1730 to 1900 on 5 October 1993. The only available ground-based radar data for this study were the WSR-88D level III low-elevation angle radar composite products (15-min intervals and 2-km resolution), which used data from the Miami (AMX), Melbourne (MLB), and Tampa Bay (TBW) radars. Several lines of thunderstorms are evident: 1) south of the keys in the Florida Straits, 2) a quasi-stationary line of convective activity along the eastern coastline of the peninsula, and 3) a line of convective and stratiform precipitation extending northeast–southwest from just north of PBI on the eastern shore, to the western coast of the peninsula. The line corresponding to FL2 and FL3 initiated before 1630 was quasi-stationary before 1700, then accelerated with a northwesterly motion of about 10 m s<sup>-1</sup>, and then began dissipating during FL3 (~1845). Individual cells that had lifetimes usually less than 30 min, were anchored to this line. The cells continually underwent evolution, and were crudely tracked in the 15-min WSR-88D composite radar data. This squall line was oriented about 30° clockwise of the 0–6-km altitude shear vector (Fig. 2b). The coastal convection overflown by the ER-2 during flight lines FL4a and FL4b began developing at 1700 and became fairly organized and intense by 1900.

### 4. General features of radar and radiometer data

#### a. EDOP observations of vertical rain structure

The EDOP time–height radar reflectivity sections from FL2, FL3, FL4a, and FL4b are shown in Figs. 3 and 4. These sections have been constructed from the EDOP beam data with 150-m vertical resolution and 2-s intervals; the heights are referenced to the nominal altitude of the section based on the radar surface return.

<sup>1</sup> Times are given in universal time coordinate (UTC). Local times are UTC - 4 h.

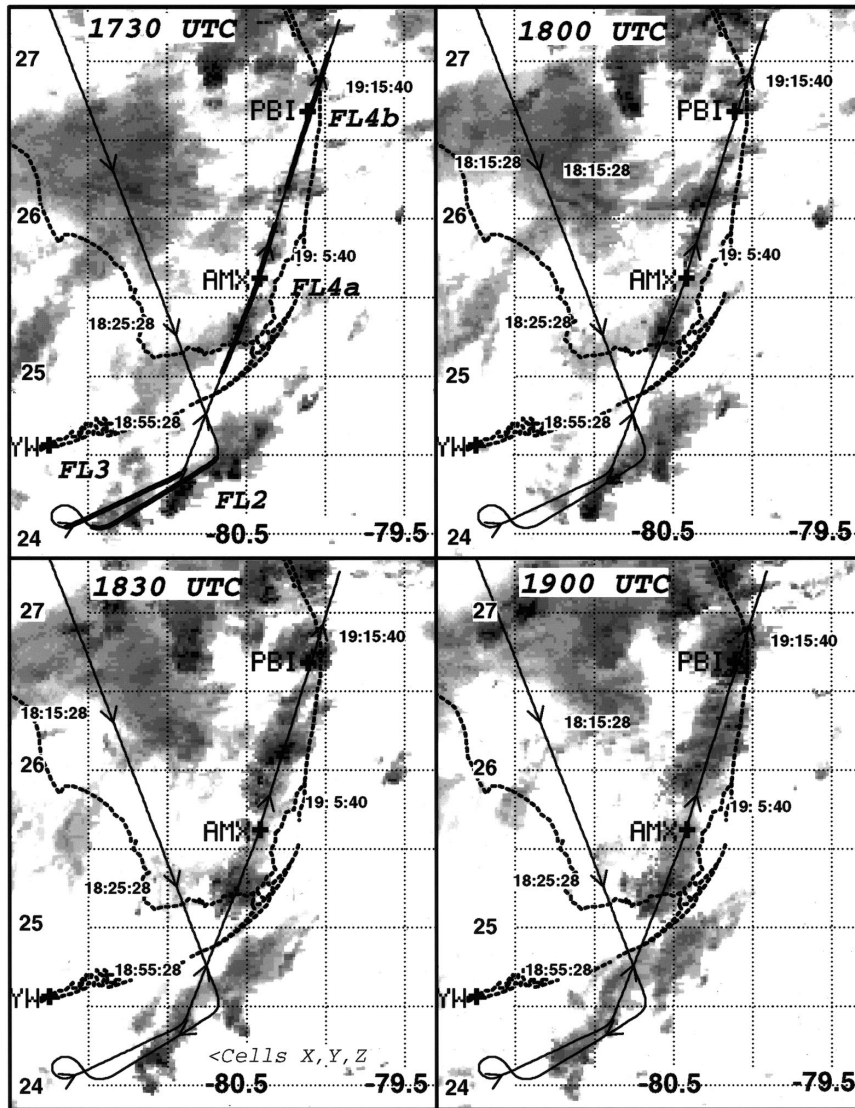


FIG. 1. Evolution of thunderstorms on 5 October 1993. WSR-88D radar composite images are shown at 1730, 1800, 1830, and 1900 UTC. Gray shades for radar data are in 5-dBZ intervals and range from 5 to 10 dBZ for lightest shades to 55–60 dBZ for the darkest shades. The overall flight track of the ER-2 (thin solid curve in all panels) and superimposed flight lines FL2, FL3, FL4a, and FL4b (bold lines in 1730 UTC panel) are indicated. Sounding locations Palm Beach (PBI) and Key West (EYW) (lower left edge) and the Miami WSR-88D (AMX) are shown. Dotted lines provide latitude, longitude grid.

A “mirror image” return similar to Meneghini and Atlas (1986) existed up to 5 km below the surface for these data but it has been omitted here to provide focus on the basic storm structure. Because the reflectivity thresholding was performed just above the noise level, some noise speckles appear in the data and should be disregarded.

The FL2 and FL3 time–height reflectivity sections (Fig. 3) cover about 70 km of aircraft translation, and there is approximately a 12-min time difference be-

tween the two flight lines. The storms had multicellular characteristics with small-scale updrafts and downdrafts, which continually evolve over time (e.g., Yuter and Houze 1995). Two storms have been identified “X” and “Y,” where X is a relatively young storm and Y exhibits high reflectivities aloft and is dissipating with heavy rain present near the surface. A third storm Z is approximately 20 km southeast of Y but is not considered here since it is off-nadir. Storm X has peak reflectivities of about 50 dBZ during FL2, and 45 dBZ

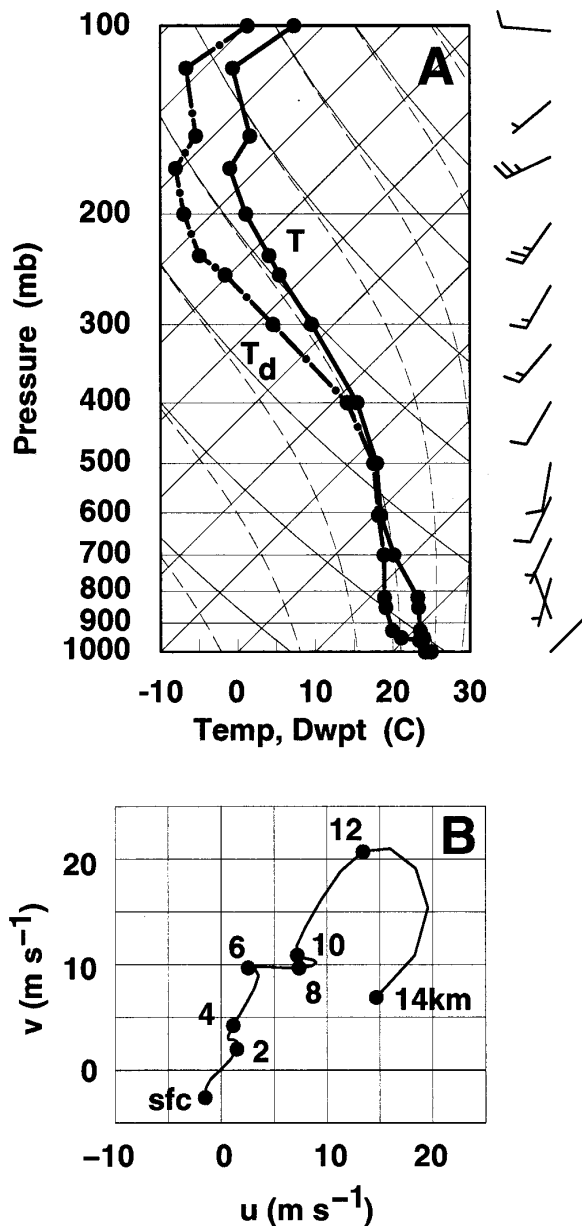
**EYW 1200 UTC 5 Oct 93**

FIG. 2. Environmental conditions associated with flight lines FL2 and FL3. Shown are (a) Key West (EYW) sounding at 1200 UTC and (b) corresponding hodograph. Wind barbs are given in meters per second; isotherms are given by thin solid lines, and pseudoadiabats are represented by thin dashed curves. EYW location is shown in Fig. 1.

during FL3. Storm Y has high reflectivities ( $\sim 50$  dBZ) near the surface during FL2 and stratiform rain with a bright band at approximately 4.4 km in FL3. During both passes, cloud-top heights were low ( $\sim 9$  km) for storm X and higher ( $\sim 12$  km) for storm Y. It is likely

that the internal structure of X and Y have undergone changes between the two overpasses of the storms, but the storms exhibit a high degree of continuity in the 10.7-GHz passive microwave measurements shown later in section 4. Also it is noted that during FL3, the ER-2 missed the center of the reflectivity cores, partly because the ER-2 typically flies over the highest cloud tops, which are not always collocated with the highest reflectivity cores and the thunderstorm updrafts. Another feature evident in the data is thin anvil cirrus from 9 to 12 km, which occurs downwind (northeast) of storm Y during FL2 (between 1833 and 1835 on the time axis in Fig. 3). This is mainly due to advection of ice particles by the  $10 \text{ m s}^{-1}$  along-track wind component corresponding to FL2 and FL3 (see EYW wind profiles in Fig. 5).

The EDOP vertical cross sections from flight lines FL4a and FL4b in Fig. 4 are constructed from observations primarily over land along the Florida coast. The rain cells depicted in the figures are associated with sea-breeze convection. A single main cell is apparent at 1858 during FL4a (Fig. 4, top panel) with peak reflectivities of about 45 dBZ extending a few kilometers above the freezing level ( $\sim 4.6$  km AGL); cloud tops extend up to 12.5-km altitude, and a bright band associated with decaying cells is observed downstream of this convective cell. This cell is tilted  $30^\circ$  from the vertical throughout its depth [toward the right in Fig. 4 (top panel) and in a north-northeasterly direction] because of the strong upper-level wind component toward the right in the cross section (see PBI along-track wind profiles in Fig. 5). The low, relatively uniform reflectivities above the bright band are consistent with previous results by investigators who found that above the freezing level vertical profiles of reflectivity in tropical oceanic convection drop off much quicker with height than for continental thunderstorm profiles (e.g., Jorgensen and LeMone 1989).

The EDOP data from FL4b (Fig. 4, bottom panel) yield evidence of many cells with dimensions of a few kilometers and in varying stages of evolution. Some of these cells are quite active: the cell observed at 1914, for example, has a high reflectivity core extending 3 km above the melting layer with peak reflectivities of 54 dBZ at 2.5-km altitude. This cell is likely to have supercooled water, based on previous studies of Florida convection (e.g., Bringi et al. 1993). The cirrus and highest cloud-top region are located about 20 km downstream of this intense cell (1915–1916), although it is likely that much of the upper-level cirrus is due to earlier convection. Similar to the main cell in Fig. 4 (top panel), the cells in this section are tilted toward the north-northeast.

Convective cells in squall lines have been shown to undergo characteristic evolution in the Tropics (e.g., Houze 1977) and more recently in Florida (Yuter and Houze 1995). Yuter and Houze have summarized typical characteristics of the evolution of Florida convec-

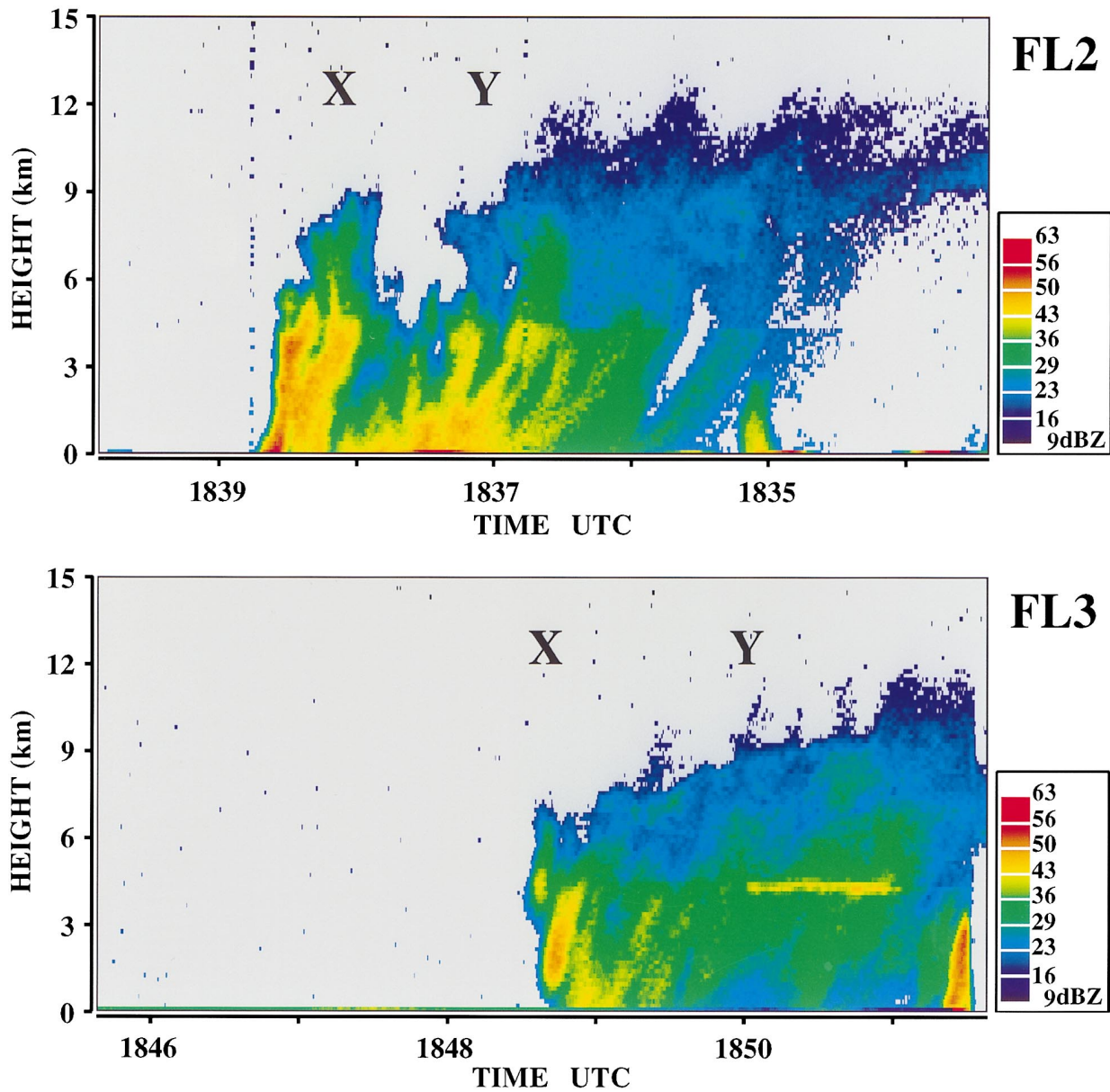


FIG. 3. Time–height reflectivity cross sections from the EDOP nadir antenna for flight lines FL2 and FL3. Heights are given relative to the surface as determined from the radar surface return. Each horizontal interval (1 min) corresponds to an aircraft translation of about 12 km. FL2 images have been flipped about the vertical axis so that time decreases toward the right to simplify comparisons with FL3 observations. Here, “X” and “Y” represent positions of storms X and Y, respectively.

tion based on radar vertical cross sections. Under vertical wind shear conditions such as those present during the 5 October 1993 CAMEX flights, new convection typically occurs on the upshear side of the thunderstorm complex, and decaying cells result in a stratiform region with a radar bright band downshear of the new cell development. The cells in FL2 and FL3 (Fig. 3) fit this description quite well, with the low- and upper-level vertical wind shear vectors pointed in the direc-

tion of the stratiform region associated with storm Y. Note that a similar two-dimensional analysis cannot be made for the storms in FL4a and FL4b because they are tied dynamically to the sea-breeze front, and the ER-2 flew parallel to this front. The thunderstorm cells studied here, which are characterized by low reflectivities above the freezing level, are consistent with warm rain coalescence processes. Previous studies (Szoke et al. 1986; Jorgensen and LeMone 1989) have found that

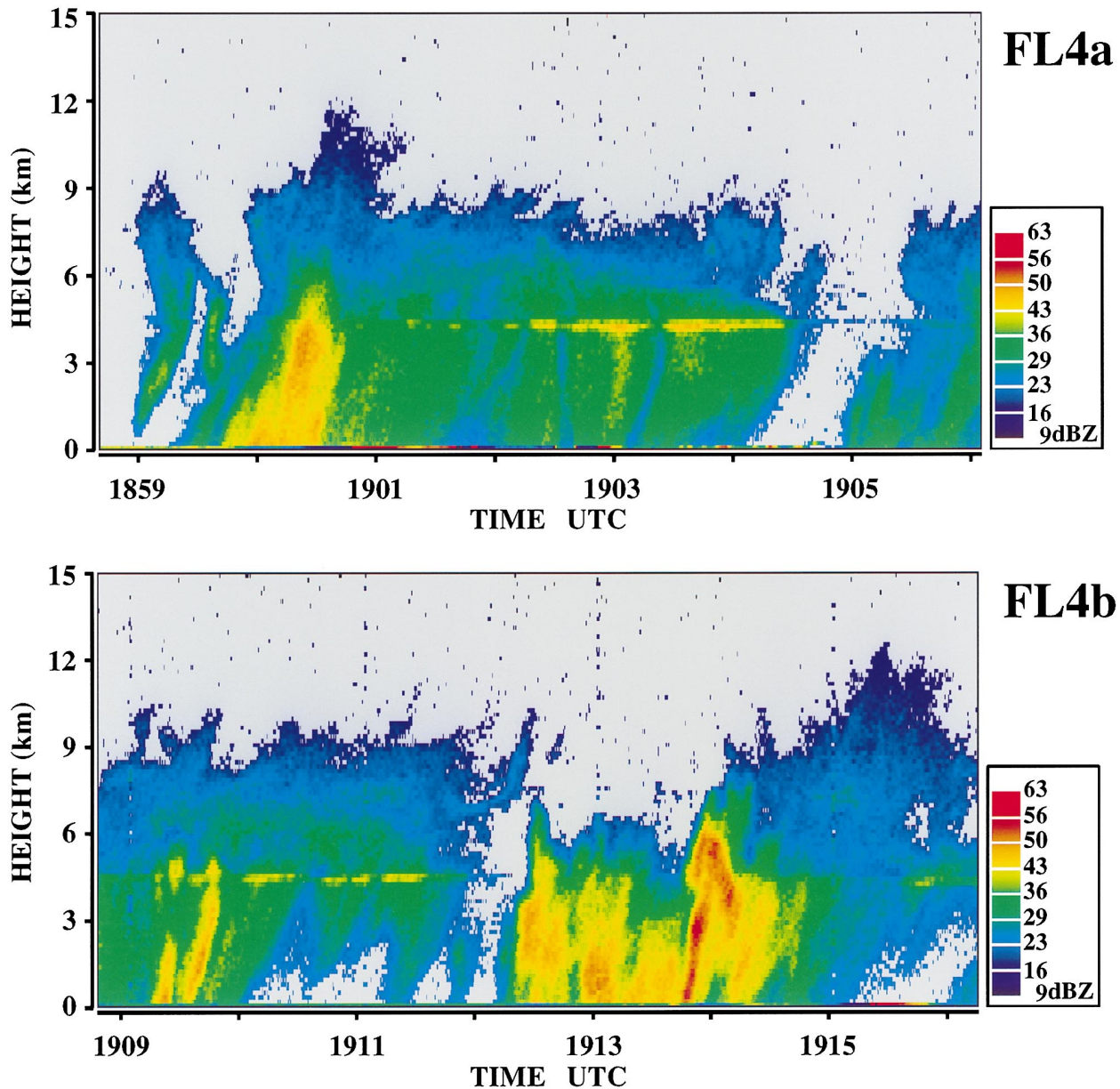


FIG. 4. Time–height reflectivity cross sections from the EDOP nadir antenna for flight lines FL4a and FL4b; otherwise similar to Fig. 3.

tropical oceanic convection during GARP Atlantic Tropical Experiment (GATE) and Taiwan Area Mesoscale Experiment (TAMEX) was characterized by weak updrafts (less than  $3\text{--}5\text{ m s}^{-1}$ ) and vertical reflectivity profiles, which decreased rapidly with height above the freezing level. Based on in situ measurements and radar reflectivities, they inferred that the rapid reduction of radar reflectivity above the freezing level was consistent with warm rain processes where weak updrafts allowed long residence times for raindrop coalescence below the  $0^{\circ}\text{C}$  level, and with rapid

conversion of cloud water to ice and graupel above the freezing level.

*b. Spatial characteristics of rain from radiometer measurements*

We now provide insight on the horizontal and vertical structure of the thunderstorms by examining the imagery provided by the passive radiometers for FL2 and FL3 (Fig. 6) and FL4a and FL4b (Fig. 7). For each flight line, the images from the AMPR (10.7,

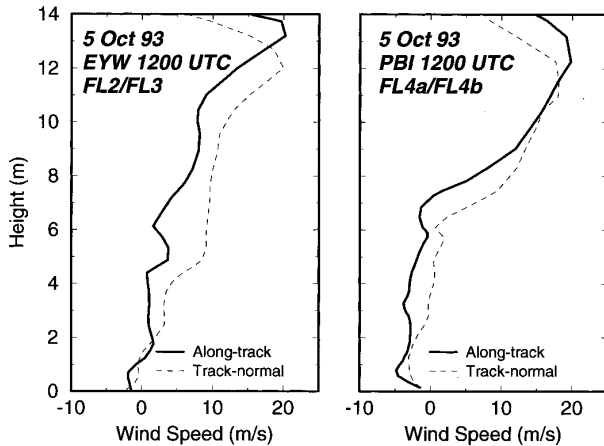


FIG. 5. Wind components along-track and track-normal corresponding to flight lines FL2 and FL3 [Key West (EYW) sounding in left panel] and FL4a and FL4b [Palm Beach (PBI) sounding in right panel]. Sounding locations are shown in Fig. 1. The along-track winds are positive in toward the right in Figs. 3 and 4; the track-normal component is directed into the page in Fig. 3 for the EYW sounding, and out of the page in Fig. 4 for the PBI sounding.

19.35, and 37.1 GHz), the MIR (89, 150, and 220 GHz), and MAMS (visible  $0.63 \mu\text{m}$  and IR  $11.12 \mu\text{m}$ ) are shown. The radiometric brightness temperatures  $T_b$  for these images are denoted by  $T_b(\text{xxx})$ , where xxx is the frequency of the measurement. Note that since the AMPR and MIR instruments have nearly identical channels at 86 and 89 GHz, the MIR channel is used through most of the paper (except in section 6) because the MIR instrument has better sensitivity. The AMPR, MIR, and MAMS measurements have been gridded to approximately the same region on the surface to facilitate intercomparisons between the multifrequency  $T_b$ 's. This procedure used bilinear interpolation and it is required since the instruments have different pixel dimensions (e.g., the MAMS data has considerably higher resolution (10 times) than that of the microwave radiometers). The surface scan swath width of the various instruments is approximately 40 km assuming an aircraft altitude of 19.5 km, and 1 min of time corresponds to about 12 km of aircraft translation. The nadir scan position, shown by the dashed line through the  $0^\circ$  scan angle, is where EDOP is viewing down to the surface (into the page). Note that more rigorous off-nadir coregistration of the images requires physical knowledge of the heights being sensed with the different radiometer channels. This is a difficult problem since the surface position of features changes off-nadir with both the scan angle and the height of the scattering or emission associated with these features; however, off-nadir coregistration is not critical for the interpretations henceforth.

The FL2 and FL3 images (Fig. 6) provide two snapshots of the storms X, Y, and Z, which were over the ocean. An ocean background provides a low micro-

wave emissivity, relatively low  $T_b$  background. In contrast, it is well known theoretically and observationally that rain emission provides a relatively high microwave  $T_b$ , which for low rainfall rates is roughly linear with rainfall rate (e.g., Wilheit et al. 1977). The thunderstorm cells for FL2 and FL3 are readily apparent in the 10.7-GHz imagery from the brightness temperature maxima due to rain emission (yellow color in 10.7-GHz panels in Fig. 6) relative to the low brightness ocean background (blue). Three storms (X, Y, and Z) are apparent in FL2 and two (X, Z) in FL3; storms X and Y along nadir were described earlier, and a third storm Z is off-nadir, and below storm Y in the figure. Note that the ER-2 did not pass directly over storm X in FL3 as mentioned earlier, and that the rain emission associated with storm Y has dissipated by the time of FL3. Progressing to higher microwave frequencies, storms X, Y, and Z are still identifiable at 19 and 37 GHz (red colors), which are still primarily emission based, while ice scattering becomes more dominant (blue colors) at 89–220 GHz. The upper-level wind shear is directed northeast (toward the right of the figure), and, thus, the ice-scattering regions in the higher-frequency microwave measurements are displaced downshear of the individual storms X, Y, and Z, consistent with the radar sections presented earlier (Fig. 3, FL2 and FL3). The visible and IR images also show a downshear displacement of the cloud tops and upper-level cirrus, but they do reveal the small ice cores present in the microwave observations. The lowest IR  $T_b$ 's ( $< 225 \text{ K}$ ) are located approximately 25 km downshear of the very active storm X in the radar measurements. This downshear displacement of the high-frequency scattering region due to vertical wind shear has been noted in previous studies (e.g., Heymsfield and Fulton 1988; Smith et al. 1994).

Previous papers have shown that low 86-GHz  $T_b$ 's are strongly correlated with radar echoes in the mid-to upper levels (6–10 km) of deep thunderstorms (12–16-km tops), because both a deep layer of ice and large ice particles are present in intense thunderstorms and the larger ice particles tend to be at lower altitudes (Hakkarinen et al. 1988; Adler et al. 1991; Heymsfield and Fulton 1988). Radiative transfer model results (e.g., Wilheit 1986) have shown that scattering results in low brightness temperatures for particles with diameters of a few hundred microns. However, graupel and hail particles with larger sizes lower the brightness temperatures significantly. Fulton and Heymsfield (1991) deduced from multiparameter radar and aircraft radiometric observations that large temperature depressions occurred [ $T_b(89 \text{ GHz}) \sim 100 \text{ K}$ ] in continental thunderstorms with centimeter-sized ice particles. On the other hand, tropical oceanic thunderstorms tend to have warmer minimum  $T_b(89 \text{ GHz})$ 's. For example, McGaughey et al. (1996) have shown from aircraft observations in TOGA

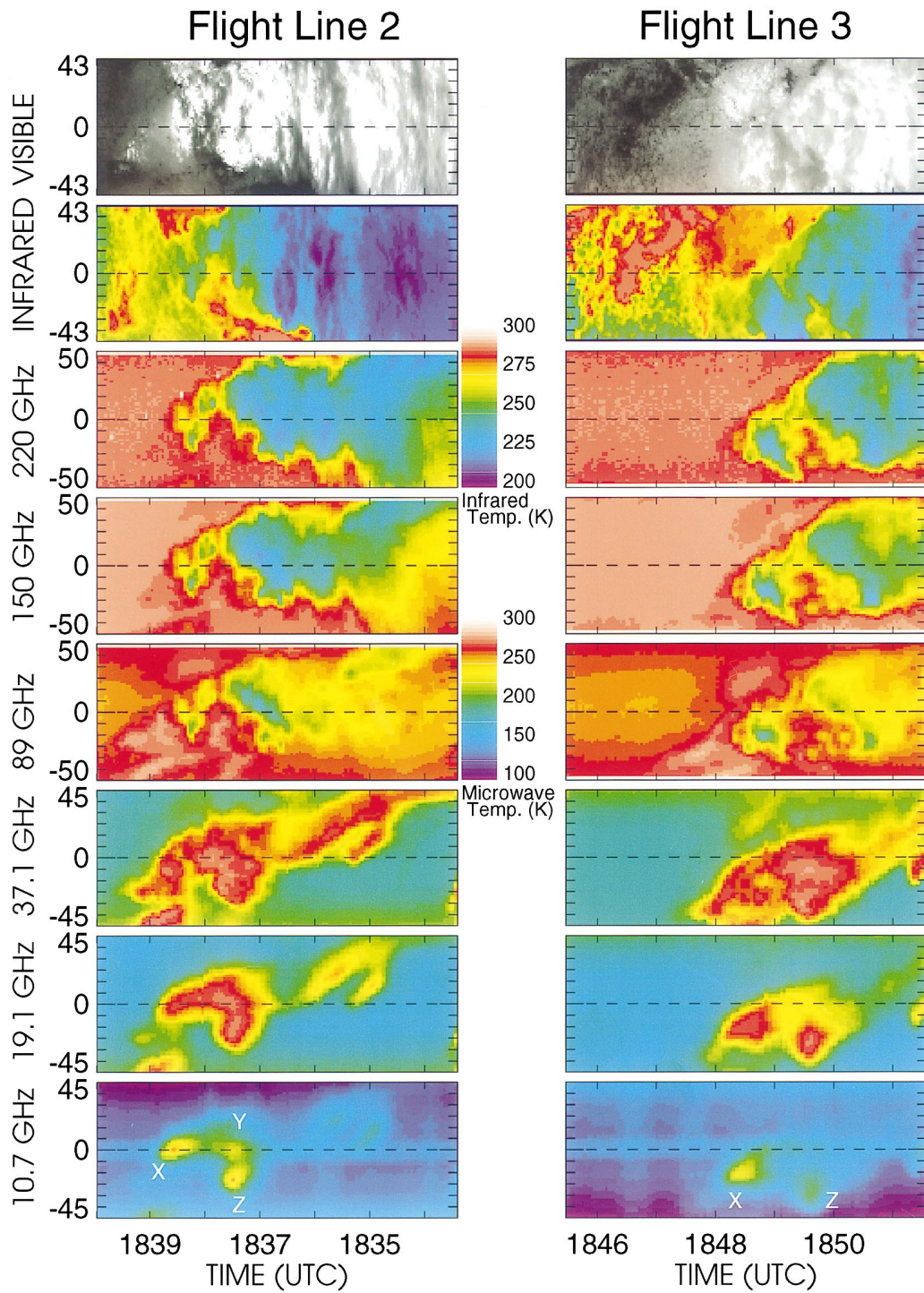


FIG. 6. ER-2 radiometric images for flight lines FL2 (left) and FL3 (right). Shown are coregistered microwave images (AMPR 10.7, 19.35, and 37.1 GHz and MIR 89, 150, and 220 GHz) and visible and infrared images (MAMS 0.6- and 11- $\mu$ m channels). Vertical axis represents scan angle in degrees. Nadir is represented by dashed horizontal line at 0° scan angle. Here, “X” and “Y” represent positions of storms X and Y, respectively.

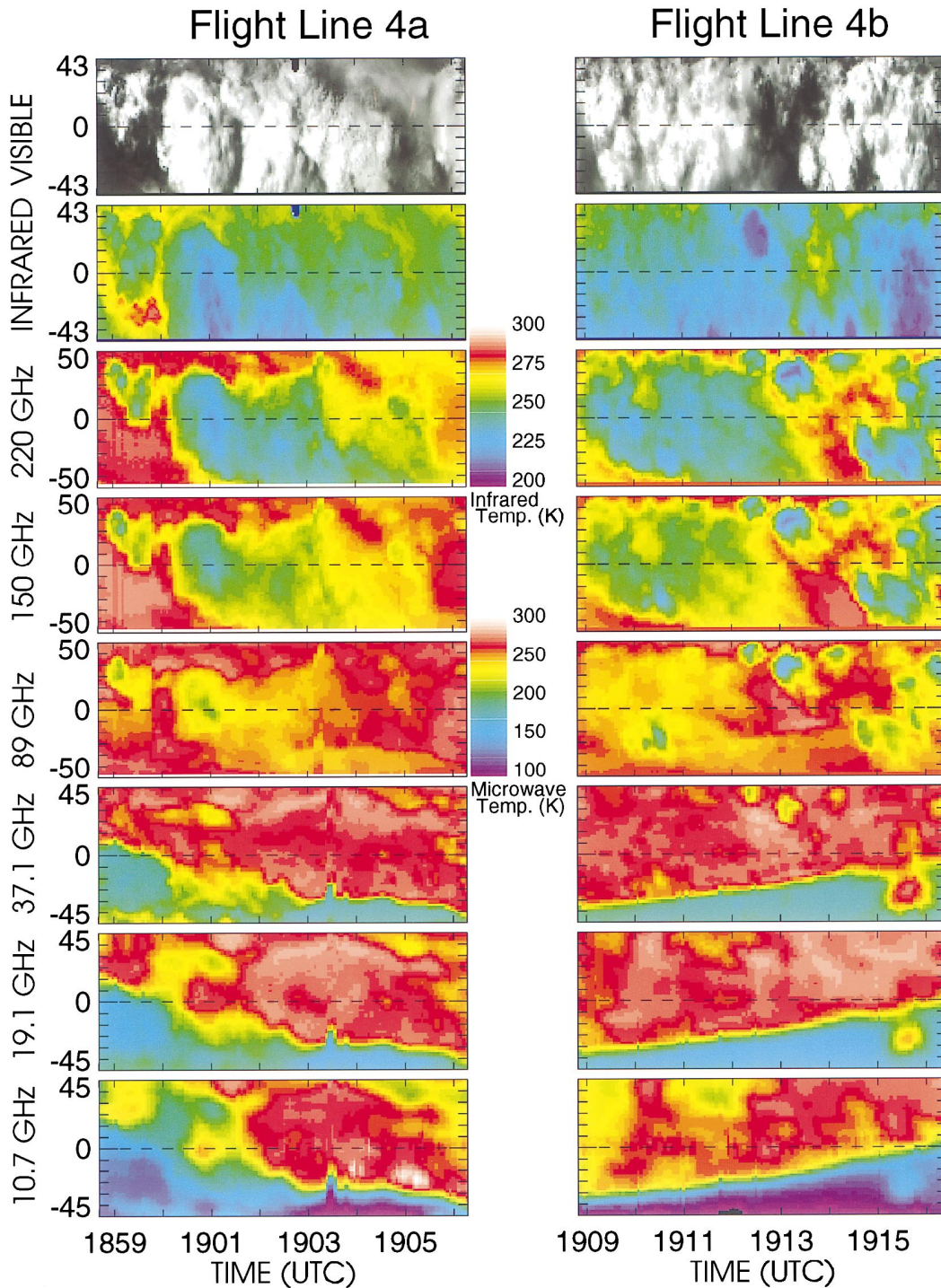


FIG. 7. ER-2 images for flight lines FL4a (left) and FL4b (right) similar to Fig. 6. The coastline of Florida is discernable by the transition between the high-emissivity land (yellow and red) and low-emissivity ocean (blue) in the 10.7-GHz panels.

COARE that the 86-GHz  $T_b$ 's rarely get below 150 K. The observations here have relatively warm  $T_b$  (89 GHz)'s and low radar reflectivities aloft,

suggesting that the ice particles may have on the average, smaller sizes as compared to continental thunderstorms of similar heights.

Several other interesting features are present in the high-frequency microwave measurements. Embedded in the ice-scattering region for off-nadir storm Z are five or six small circular regions of lower  $T_b$ 's at 89 GHz, each less than 2 km across (embedded yellow regions at 1850 in the 89-GHz panel, Fig. 6). These features suggest individual ice cores possibly associated with small-scale updraft pulses comprising storm Z, which was previously identified in the 10.7-GHz imagery. Interestingly, the higher-frequency measurements associated with storm Z indicate a general lack of scattering (red shades are characteristic of atmospheric absorption at frequencies of 89 GHz or larger). Resolution is key here because the 89-GHz MIR data (or 86-GHz AMPR data) have greater than a factor of 5 higher resolution with respect to the 10.7-GHz AMPR measurements, which have a surface footprint of 2.8 km. The IR data from FL3 give evidence (although not discernible in reduced resolution data shown in the figure) of small-scale cloud towers associated with storm X. We surmise from the radiometric observations that the storms are composed of many discrete small (few kilometers) updraft elements in varying stages of development. Small-scale updraft pulses often go undetected in ground-based radar azimuthal scans but in situ measurements from aircraft penetrations [e.g., from TAMEX tropical convection; Jorgensen and LeMone (1989)], have shown that updrafts have median diameters on the order of a kilometer.

The radiometer images from FL4a and FL4b, which are mostly over land (Fig. 7), require a different interpretation than the oceanic thunderstorms just described. It is well known (e.g., Spencer 1984) that rain emission is difficult to detect over land because of the lack of contrast between the warm rain emission and the high emissivity (warm) land background (e.g., Simpson 1988). Detection of rain over land is best accomplished indirectly by using the higher-frequencies to sense the ice scattering region often found above the rain region (e.g., Adler et al. 1993). Segments of FL4a and FL4b demonstrate the limitations of passive microwave measurements over land. It should be noted that the very beginning of FL4a and the tail end of FL4b were over water (dark blue shades at 10.7 GHz in Fig. 7), so that the background temperatures will be much lower in these regions. The main cell observed during FL4a (previously described) at 1901 was over water and the stratiform region just to the north (to the right in figure) was over land at nadir (cf. FL4a in Figs. 4 and 7). For some of the high rain-rate rain regions over the land segments, the  $T_b$ 's at the lower microwave frequencies (Fig. 7, 10.7 and 19.1 GHz) are lower than the emission from the earth's surface, but this background emission itself is highly variable due to varying soil moisture, surface vegetation, etc. For example, an embedded area of lower 10.7- and 19.35-GHz  $T_b$ 's is detected at 1903 (darker red shades at nadir) over the warmer

(red/white) background. This more intense rain region correlates with the stratiform rain and bright band region observed by the EDOP radar (FL4a in Fig. 4). This lack of contrast between the rain and land emission indicates the difficulty in rain estimation over land using emission-based microwave frequencies.

In contrast to the emission-based measurements, the low  $T_b$ 's in Fig. 7 at greater than 37 GHz and the IR temperatures (Fig. 7, low  $T_b$ 's in 11  $\mu$ m panel) define the ice region associated with convective and stratiform rain over land. However, these ice regions are down-shear of the main convective cell at 1901 during FL4a (see radar data in Fig. 4), similar to the oceanic convection during FL2 and FL3. This is due to advection of ice particles by the strong winds aloft indicated in the PBI sounding (Fig. 5), which are toward the northeast and slightly to the right of the flight line (down in Fig. 7). The images from FL4b (Fig. 7) show somewhat more complicated structure in the microwave channels, with numerous small cells off-nadir and a cell just off the coastline at 1915:30. The most intense cells in the images are off-nadir and are readily apparent from the large amount of ice scattering at frequencies above 37 GHz and the low IR  $T_b$ 's associated with high cloud tops. One interesting example is the relatively intense cluster of cells observed between 1912 and 1914 in the EDOP observations (Fig. 4) at frequencies above 37 GHz (Fig. 7, right panels); these cells have no discernible low-frequency (<37 GHz)  $T_b$  features associated with them. Yet, some of the off-nadir cells appear to be quite strong since  $T_b$ 's are less than 200 K at 37.1 GHz, which are too low for rain emission and, thus, imply that ice scattering is likely present (e.g., Spencer et al. 1989; Smith et al. 1994). Thus, the limitations of using emission-based microwave frequencies over land backgrounds are clearly shown in these observations.

## 5. Implications of observations on rain estimation approaches

### a. Oceanic thunderstorm

#### 1) DISCUSSION OF OBSERVATIONS

Over the ocean, it is well known that  $T_b$ 's at the lower frequencies increase rapidly with increasing rainfall rate up to a certain rainfall, and then decrease at higher rainfall rates. This critical rainfall rate decreases with increasing frequency, and results from the fact that the rain layer becomes opaque at a lower rainfall rate as the frequency increases (e.g., Olson 1989). Smith et al. (1994) recently concluded from a rain retrieval method applied to AMPR multifrequency measurements that the 10-GHz channel improves the rainfall measurements significantly because the 19-GHz channel often saturates in heavy rain. The oceanic flight lines FL2 and FL3 presented here provide the opportunity to validate passive microwave precipitation re-

trieval methods such as the Kummerow and Giglio (1994) physical approach and the scattering technique of Adler et al. (1993), as well as combined passive-active microwave methods such as Olson et al. (1996). Precipitation retrievals on this oceanic dataset will be described in Kummerow et al. (1995) and Olson et al. (1995). The multifrequency observations are examined here at nadir to determine their response to rain and other features of the observations.

The nadir profiles of radiometric and radar data from FL2 and FL3 are presented in Figs. 8 and 9, respectively. Some of the features in these profiles are evident in the images discussed in the previous section, but the nadir profiles here provide an opportunity to relate the radar and radiometric information directly. Similar pro-

files have been presented in previous papers using ER-2 radiometric and ground-based radar data (Heymsfield and Fulton 1988; Hakkarinen et al. 1988) and with DC-8 radar and microwave radiometric data from 10 to 90 GHz (Wang et al. 1994). The profiles here have been constructed from the 0° scan angle radiometric measurements and from EDOP range-gated nadir profiles. Panels (a) and (b) show the AMPR and MIR data, respectively, while panel (c) shows the MIR 220-GHz channel and the MAS 11-μm IR channel. The EDOP panel (d) shows the reflectivity values in the 0.45-km range gate (closest usable gate to the surface), and the layer averaged reflectivities in the rain region (0.4–4-km altitude) and the ice region (6–10-km altitude). Panel (e) gives the rainfall rate calculated us-

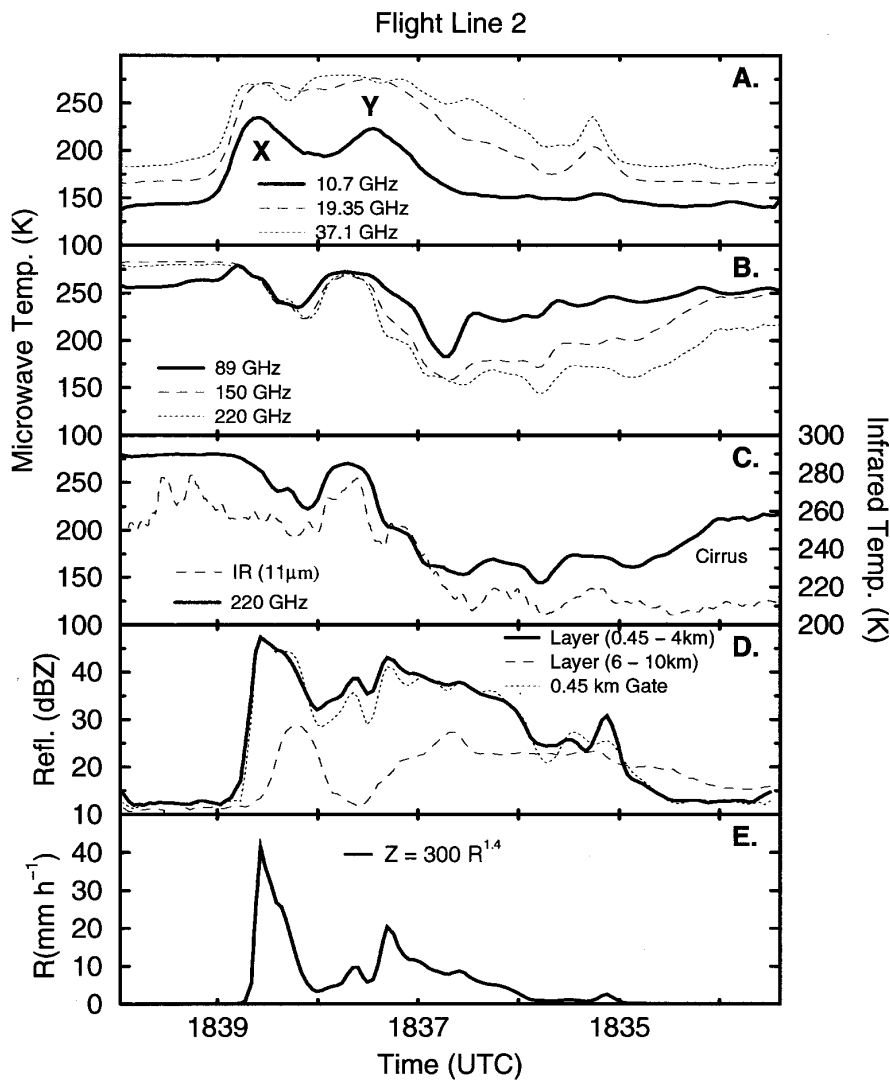


FIG. 8. Profiles of radiometric and radar data for flight line FL2 along nadir (horizontal dashed line in Fig. 6). Shown are passive microwave (panels a, b, and c), infrared (panel c), EDOP reflectivities (panel d), and rainfall rates derived from EDOP radar data (panel e). Storms X and Y are labeled in (a).

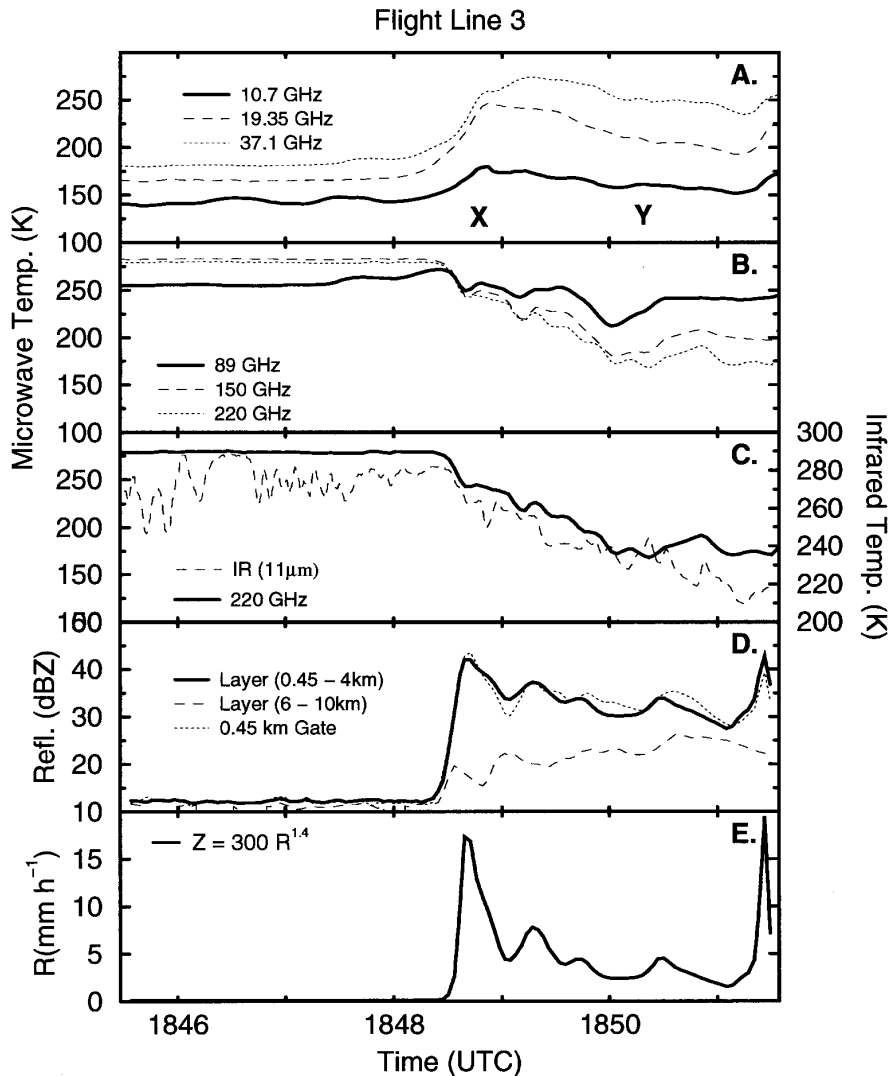


FIG. 9. Profiles of radiometric and radar data for flight line FL3 along nadir (horizontal dashed line in Fig. 6); otherwise similar to Fig. 8.

ing the Miami  $Z$ - $R$  relation after Woodley and Herndon (1970), who used rain data from the Florida Area Cumulus Experiment (FACE). This relation is given by  $Z = 300 R^{1.4}$ , where  $Z$  ( $\text{mm}^6 \text{m}^{-3}$ ) is the radar reflectivity factor,  $R$  ( $\text{mm h}^{-1}$ ) is rainfall rate; the WSR-88D operational radars also use this same relation because of its general applicability. In the current study,  $Z$  is the 0.45-km altitude EDOP radar reflectivity factor. Note that the data are plotted as raw unfiltered values from each instrument. Also, the aircraft roll angles are generally very small (less than  $1^\circ$ ) over the flight tracks, and so this angle has not been factored into the microwave brightness temperature profiles. The beamwidths of the microwave radiometers and the EDOP are fairly large compared to any pointing differences between the instruments, and so roll angle is not con-

sidered to be an important factor here. However, it is noted that the beamwidths of the microwave instruments vary greatly, as described earlier. The AMPR 10.7-GHz channel has a beamwidth approximately 2.5 times that of the EDOP. This lower spatial resolution of the AMPR causes greater filtering of small-scale features such as convective rain regions. One beamwidth for the lowest-resolution AMPR 10.7-GHz channel corresponds to approximately 12 s of time on all figures in this paper.

The FL2 and FL3 profiles (Figs. 8 and 9) indicate the various interrelations between the microwave and IR signatures and vertical precipitation structure. Storm X during FL2 has a peak reflectivity, rain rate, and  $T_b$  (10.7 GHz) of 53 dBZ,  $70 \text{ mm h}^{-1}$ , and 235 K, respectively; storm Y has corresponding peak values of

48 dBZ, 40 mm h<sup>-1</sup>, and 225 K. The peak  $T_b$ 's (10.7 GHz) for storm X and storm Y during FL2 indicate higher  $T_b$ 's are correlated with higher rainfall rates (cf. Figs. 8a and 8e) as expected from previous radiative transfer modeling results (e.g., Olson 1989). Also, the  $T_b$ 's at 19.35 and 37.1 GHz associated with storms X and Y are saturated ( $\sim 275$  K) because of the greater radiative opacity of rain at these frequencies. The region of peak rainfall rate associated with storm X (between 1838 and 1839 in Fig. 8) covers about 30–60 s on the timescale, which is equivalent to a cell width of 5–10 km (1 min on the time axis corresponds to about 12 km of aircraft translation). The smoothing out of this rain cell is evident at 10.7 GHz, which has the lowest resolution. The rainfall rate profiles in Figs. 8e and 9e show the apparent weakening of storm Y detected earlier in the radiometric imagery in Fig. 6, with rainfall rate decreasing from a peak value of approximately 20 mm h<sup>-1</sup> during FL2 to less than 5 mm h<sup>-1</sup> during FL3. It is obvious from these profiles that the low-frequency (particularly 10 GHz) passive microwave measurements detect the rain cells quite well. On the other hand, the higher-frequency measurements, which are sensitive to ice scattering, are not well correlated with the rain amounts from these storms. The  $T_b$  (89 GHz) minima associated with storms X and Y during FL2 (Fig. 8b) are located downshear of the convective regions and the EDOP-derived surface rainfall rates (Fig. 8e). Storm Y, which has lower rainfall rates than storm X, exhibits a  $T_b$  relationship, which is the opposite to what is expected; that is, storm Y has a lower  $T_b$  (89 GHz) than storm X. The passive measurements at frequencies above 37 GHz become ambiguous because the signal comes mainly from scattering in the ice layer and not from rain near the surface (e.g., Wilheit 1986).

SSM/I passive microwave rain retrievals over land rely on the use of the 86-GHz channel, which responds well to larger ice particles often found aloft in continental thunderstorms (e.g., Adler et al. 1993). The main advantage of the scattering-based algorithms which use the 86-GHz channel data are that the spatial resolution of these data are significantly higher compared to the low-frequency measurements (SSM/I resolution is approximately 40 km at 19 GHz and 12 km at 86 GHz), and that scattering at 86 GHz yields a greater  $T_b$  contrast over land than the emission signal at the lower microwave frequencies. The Goddard scattering algorithm (GSCAT) uses the horizontally polarized  $T_b$  (86 GHz) to define rain intensity over land and water (Adler et al. 1993). The approach uses the scattering signal due to the presence of ice aloft in precipitation systems, to indirectly assign rainfall amounts. Earlier analysis of convective cells in this paper indicates that even the SSM/I 86-GHz beamwidth is relatively large in comparison with the dimensions of ice cores in thunderstorms. The GSCAT relations are tuned for the much lower resolution SSM/I measurements

and not for the higher-resolution aircraft measurements presented here.

Storm evolution in the tropical convection studied here has important implications for the interpretation of passive microwave measurements and the application of rain retrieval methods. Observations presented here are consistent with warm rain coalescence processes as described in previous literature with rapid glaciation of supercooled water and a predominance of ice hydrometeors above the freezing level (e.g., Jorgensen and LeMone 1989). Also, weak updrafts are likely in this case since high reflectivities do not extend much above the freezing level. If updrafts are indeed weak, many of the larger hydrometeors fall out of updraft region and smaller ice particles remain aloft to be detrained and advected downshear of the cells by the upper-level winds. These observations are consistent with earlier studies (Fulton and Heymsfield 1991) from midlatitude convective storms, which showed that storm evolution resulted in the surface rainfall in their study lagging the minimum 90 GHz and IR brightness temperatures because of the additional time it takes the ice particles to fall to the surface from higher altitudes.

Since the 11- $\mu$ m IR  $T_b$ 's (Figs. 8c and 9c) are observed to roughly parallel the higher frequency ( $> 89$  GHz) microwave measurements (Figs. 8b and 9b), they are also poorly correlated with the rain regions present in the radar images (Fig. 3) and the emission-based brightness temperature depressions in the 10.7-GHz microwave measurements (Figs. 8a and 9a). The IR  $T_b$ 's for FL2 (Fig. 8c) indicate roughly a 240-K brightness temperature minimum over the weaker storm Y, while storm X has a 250-K minimum. Quantitative rain estimation is difficult here using IR measurements because the coldest IR  $T_b$ 's are considerably downwind of the convection and surface rainfall. The scattering-based  $T_b$ 's (particularly 86 GHz) are better than the IR for rain detection since they are less sensitive to nonprecipitating clouds than the IR, although measurements at frequencies greater than 89 GHz tend to approach the IR data. This is evident in the IR measurements, which have more fluctuations than the microwave measurements, particularly in the 1846–1848 period during FL3 (Fig. 9). Before 1835 in FL2 (Fig. 8), the IR profile has uniformly low  $T_b$ 's, because the IR is responding to the high cirrus layer. The microwave  $T_b$ 's at 86 GHz are fairly insensitive to the high-level ice region; however,  $T_b$ 's at 150 and 220 GHz detect the cirrus since they increase in this same region. Clearly, the IR responds to thin cloud layers, and in FL3, low-level stratocumulus (see Fig. 9 between 1846 and 1848). This may lead to erroneous conclusions regarding rain below. In contrast, results here and in previous observational studies have shown these low and midlevel clouds produce negligible scattering and emission at the microwave frequencies (e.g., Heymsfield and Fulton 1988).

## 2) COMPARISON OF DATA WITH RADIATIVE TRANSFER CALCULATIONS

Previous theoretical studies have shown, based upon radiative transfer calculations, the sensitivity of the brightness temperature–rainfall rate relationship to other parameters such as ocean surface wind speeds, beam filling, fractional coverage, and rain-layer depth (e.g., Wilheit et al. 1977; Olson 1989). Here, we are interested in the degree to which brightness temperatures correlate with rainfall rate. For this purpose, the coincident radar and the AMPR 10.7–37 GHz and 86-GHz MIR radiometer observations from FL2 and FL3 are used to examine single frequency  $T_b$ –rainfall rate relationships. The AMPR, MIR, MAS, and EDOP data are sampled at different times, and they have different spatial resolutions. Thus, a combined dataset was constructed by interpolating the EDOP, MIR, and MAS datasets to the lowest spatial resolution ( $\sim 2.8$  km at 10.7 GHz) AMPR measurements at 3-s intervals. The reflectivities were first thresholded at 15 dBZ ( $0.6$  mm h $^{-1}$  rainfall rate) and then smoothed using a five-point running average (12 s elapsed time or about 3 km of aircraft translation). The radiometer data were smoothed using a three-point running average (6 s). This procedure provided smoothing of the finer-scale radar measurements and reduced small-scale noise fluctuations present in the datasets. A layer reflectivity and rainfall rate are used here for comparison with the microwave  $T_b$ 's since the lower-frequency radiometric measurements respond mainly to the path-integrated liquid precipitation (and, thus, the integrated rainfall rate or reflectivity) along the radiometer line of sight. A mean layer-rainfall rate has been calculated from the EDOP layer-mean (0.45–4 km) reflectivities using the Miami  $Z$ – $R$  relation described earlier in this section.

Figure 10 presents  $T_b$  versus rainfall rate for FL2 and FL3 using the 10.7, 19.35, 37.1, and 86 GHz AMPR brightness temperatures and the collocated EDOP layer rainfall rates. The scatter of EDOP rainfall rates and 10.7-GHz AMPR  $T_b$ 's in the FL2 data can be partly attributed to the fact that the 10.7-GHz AMPR channel data are relatively low resolution ( $\sim 2.6$ -km footprint), and, therefore, the radiometric signal is contaminated by nearby high-brightness precipitation cores, whereas the higher-resolution EDOP footprint ( $\sim 1.1$  km) may be nearly rain-free. The mismatch of instrument footprints has the effect of producing relatively high  $T_b$ 's at low reflectivities (see also Figs. 8 and 9). Although some scatter in the plots is instrument or analysis related, it should be noted that natural variations in humidity, nonprecipitating cloud water, precipitation horizontal and vertical structure, and surface wind speed can also contribute to scatter in the data. In spite of some scatter, the 10.7–37.1-GHz plots generally increase monotonically with increasing rainfall rate (and reflectivity) and then level out or even decrease slightly beyond a given rainfall rate. Also note that the rainfall

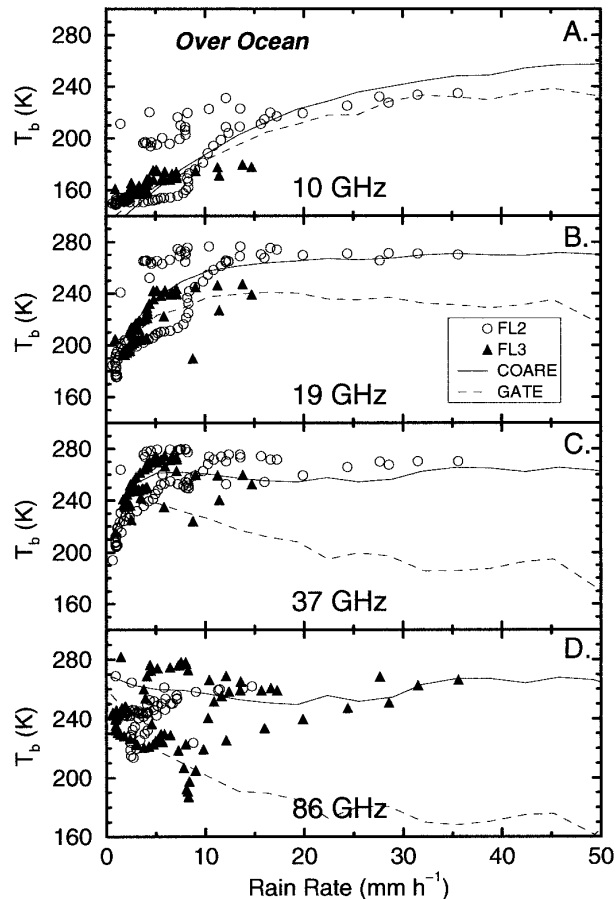


FIG. 10. Microwave  $T_b$ 's vs EDOP-calculated rainfall rate for oceanic flight lines FL2 and FL3. Observations are given for 10.7 GHz (A), 19.37 GHz (B), 37.1 GHz (C), and 86 GHz (D). Each symbol represents a radar reflectivity–radiometric  $T_b$  pair from the observations. The “COARE” and “GATE” curves were obtained from cloud and radiative transfer modeling calculations.

rate at which the emission signal saturates, decreases with increasing frequency. The 10.7-GHz data saturates (i.e., peaks or levels off) at about 30 mm h $^{-1}$  ( $\sim 45$  dBZ), while at 19.37 and 37.1-GHz, brightness temperatures saturate at roughly 7 mm h $^{-1}$  ( $\sim 37$  dBZ) and 3 mm h $^{-1}$  ( $\sim 31$  dBZ), respectively. Wilheit et al. (1977), Olson (1989), and others have modeled this saturation behavior, which shows a decrease of the  $T_b$ 's above the saturation rainfall rate for certain conditions. This saturation rainfall rate depends on the optical extinction coefficient, which is a function of the depth of the rain layer, the liquid water content, and the size distributions of the raindrops. Figure 10 shows that scattering-based  $T_b$  (86 GHz) has weak dependence on rainfall rate in part because of the horizontal displacement of the ice-scattering region from the rain region; this was attributed to vertical wind shear earlier in the discussion.

The experimental data are now compared to theoretical curves plotted in Fig. 10 based on numerical cloud and radiative transfer models. The Goddard cumulus ensemble (GCE) model was utilized to provide microphysical inputs to a microwave radiative transfer model. Previous simulations from tropical environments observed during the GATE and the TOGA Coupled Ocean–Atmosphere Response Experiment are used for this purpose. The reader is referred to numerical modeling results by Tao and Simpson (1989) and W.-K. Tao (1995, NASA/Goddard Space Flight Center, personal communication) for detailed descriptions of the GATE and TOGA COARE simulations, respectively. These simulations are used here because the microphysical parameterizations have been studied in detail and the environments from the GATE and TOGA COARE simulations share similarities, although are not identical to the CAMEX observations. The grid resolution of the GATE simulation was 1500 m in the horizontal, and between 230 and 1000 m in the vertical; for TOGA COARE the resolution was 1000 m in the horizontal and similar to the GATE resolution in the vertical. The three-dimensional cloud water and precipitation fields are provided at five different times (126, 138, 174, 210, and 234 min) in the GATE simulation and at eight different times (30, 60, 90, 120, 150, 180, 210, and 240 min) in the TOGA COARE simulation.

A radiative model, based upon Eddington's second approximation (Weinman and Davies 1978), is used here to calculate the brightness temperatures upwelling from the vertical profile of hydrometeors provided by the cloud model at each horizontal gridpoint. Thus, a large ensemble of high-resolution ( $\sim 1$  km) nadir-look brightness temperatures is obtained for both the GATE and TOGA COARE simulations. Nadir-look brightness temperatures are calculated for each of the microwave frequencies (10.7, 19, 37, and 86 GHz). Similarly, reflectivities at the EDOP frequency of 9.72 GHz, including the two-way path attenuation from the ER-2 altitude and the precipitation target, are simulated based upon the precipitation distributions produced by the cloud model. The simulated rainfall rates are vertically integrated up to 4.5-km altitude to create mean rainfall rates comparable to the ones plotted in Fig. 10.

To create the curves in Fig. 10, the brightness temperature simulations from both GATE and TOGA COARE were subdivided into 21  $0.11 \text{ g m}^{-3}$  precipitating liquid water intervals between 0.0 and  $2.3 \text{ g m}^{-3}$  to provide a representative average of brightness temperatures within each interval without altering the shape of the  $T_b$ –rainfall rate curve. The brightness temperatures and rainfall rates corresponding to the cloud model profiles in each interval were averaged and plotted. Curves are then drawn to connect the plotted points.

It may be noted from the figure that there is a rough correspondence between the aircraft-observed brightness temperature data and the theoretical curves. A sig-

nificant scatter of data about the curves is also evident, but it should be recognized that the theoretical curves represent mean relationships between the brightness temperatures and rainfall rate, and that individual cloud model profiles can produce significantly different brightness temperatures for a given rainfall rate. The systematically lower GATE brightness temperatures reflect the generally larger proportion of ice precipitation (snow and graupel) with respect to rainfall in the GATE simulation. The reason for this is that the GATE simulation produces deep, nearly vertical convective cells, while the TOGA COARE simulation yields cells with significant tilt and relatively low cloud tops.<sup>2</sup> It may be noted from Fig. 3 that the precipitation cells from FL2 and FL3 have significant tilt, with significant precipitation mainly limited to altitudes below 9 km. Therefore, there is a greater similarity between the observed cells and those simulated for the TOGA COARE environment.

#### *b. Thunderstorms and stratiform rain over land*

An important question for satellite rain estimation by passive microwave techniques is how well rain can be detected and estimated over land. FL4a and FL4b are typical of Florida sea-breeze convection and provide a unique opportunity to examine the remote sensing aspects of these primarily land-based thunderstorms. The availability of simultaneous collocated radar measurements greatly enhances this analysis. Figure 11 shows FL4a profiles that cover the convective region (about 10 km across at 1900–1901) and the trailing stratiform region discussed previously (these are both identified in Fig. 11a). The precipitation for this line spans from over ocean to over land and shows the ambiguities introduced in the interpretation of microwave  $T_b$ 's in these transition regions. The convective region, which is mainly over the ocean, has peak rainfall rates of  $35 \text{ mm h}^{-1}$  and peak reflectivities of 48 dBZ at the surface and in the lower troposphere. The corresponding  $T_b$  (10.7 GHz) in Fig. 11a is approximately 250 K, which is very strong rain emission compared with the low-emissivity ocean background (surface emission in clear air  $T_b \sim 140 \text{ K}$ ). Smith et al. (1994) have observed  $T_b$  (10.7 GHz)'s due to rain emission of similar magnitude ( $\sim 260 \text{ K}$ ) during flights over deep convection in the northeastern waters of the Gulf of Mexico. On the other hand, the stratiform region shows relatively level  $T_b$ 's (10.7–37.1 GHz) with 5–10-K variations after

<sup>2</sup> These differences may be due to the use of different initialization and boundary conditions between the simulations. The GATE simulation was made using an older version of the GCE model with periodic boundary conditions and deep tropospheric lifting, whereas the COARE convection was simulated using an updated version of the model with open lateral boundary conditions and much less vertical ascent.

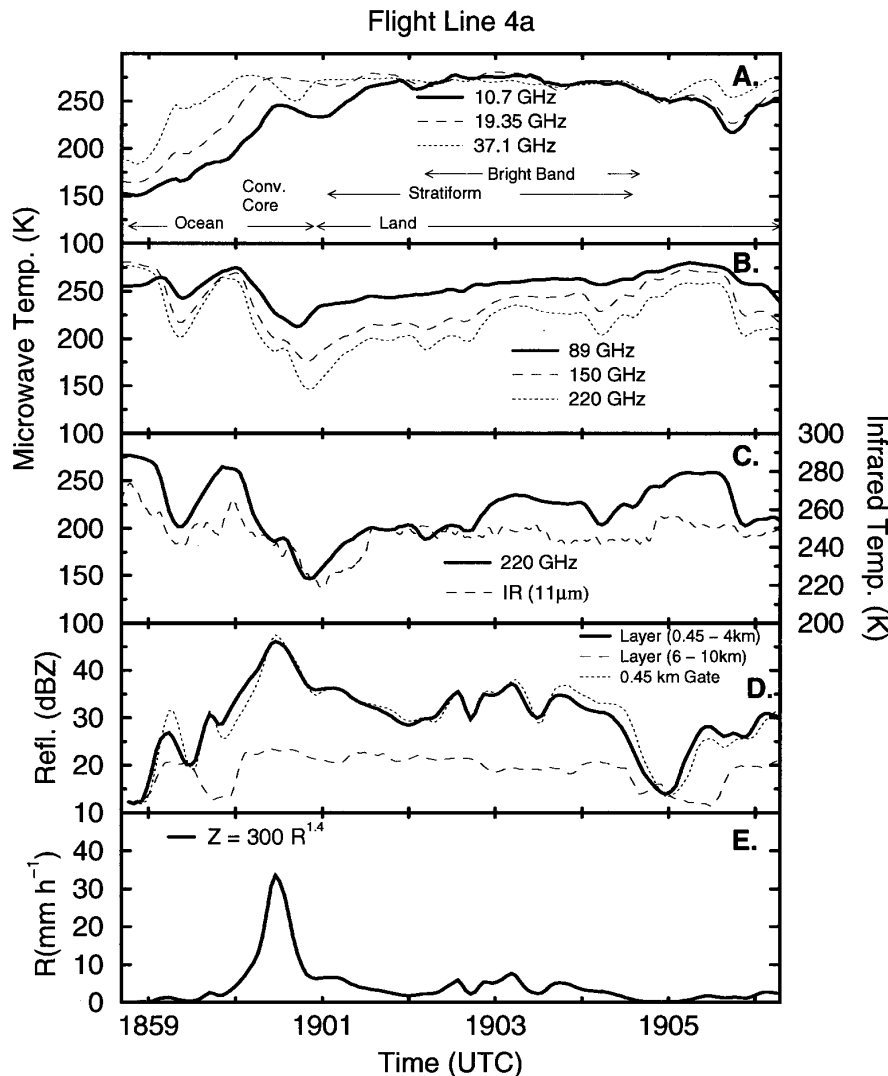


FIG. 11. Profiles of radiometric and radar data for flight line FL4a along nadir (horizontal dashed line in Fig. 7); otherwise similar to Fig. 8.

1902, suggesting the difficulties of rain estimation over land. Variable surface emissivity resulting from vegetation and soil moisture rather than rain could be responsible in part for the  $T_b$  variability of the aircraft measurements over land. Some of these surface effects can be reduced using polarization measurements at lower frequencies ( $<19$  GHz), which unfortunately were unavailable during these flights. Wet soil acts similar to an ocean surface, causing large polarization differences between the horizontal and vertical polarized channels, whereas highly vegetated regions tend to produce much lower polarization differences (e.g., Spencer et al. 1989; Heymsfield and Fulton 1992).

Ice scattering is evident in the  $T_b$ 's at 89 GHz and higher frequencies throughout the stratiform region (i.e., the cloud-free  $T_b$ 's are somewhat warmer than the

$T_b$ 's observed here), but this ice region is displaced considerably from the surface rain region. The 89-GHz minimum of approximately 215 K associated with the convective region (1900–1901 in Fig. 11b) is displaced 4 km (or 20 s on the time axis) downwind of it; the higher-frequency features (140 K at 220 GHz) are displaced progressively farther downwind in accord with the tilt of the reflectivity core in Fig. 4. Unlike the microwave observations, the  $T_b$  (11  $\mu\text{m}$ ) identify the convective core similar to the 220-GHz observations, but they are fairly constant ( $\sim 250$  K) over the stratiform region. The IR  $T_b$ 's represent near cloud-top temperatures due to the strong absorption by the ice particles at this short wavelength. The high-frequency microwave data are sensitive to ice scattering from much larger ice particles and consequently penetrate farther

into the cloud. However, while both IR and higher-frequency microwave measurements identify the convective region in the difficult land–ocean transition region (although displaced from the surface rainfall), neither perform well in the stratiform region. For example, the region with the most prominent bright band (1902–1905) and the radar-estimated rainfall rates of  $5 \text{ mm h}^{-1}$ , do not correlate particularly well with any of the radiometric measurements.

Similar ambiguities are observed from the FL4b profiles (Fig. 12), which are characteristic of typical mid-afternoon sea-breeze-generated convection just inland of the coast. The rainfall-rate profiles (Fig. 12e) indicate two regions of land-based thunderstorms at approximately 1909–1911 and 1912–1915 with peak rainfall rates of about 18 and  $45 \text{ mm h}^{-1}$ , respectively.

These regions are approximately 12 and 36 km across, respectively. As noted earlier, each of these regions is composed of smaller cells approximately 3 km across. The most intense cell is at 1914 just before the land–ocean transition. The two intense rain regions have relatively poor response in the low microwave frequencies again because of a lack of contrast between rain and surface emission. There is 25-K lowering of the  $T_b$  (10.7 GHz)'s in the convective regions (about 1909 and 1914), and 10 K of  $T_b$  (10.7 GHz) lowering in the stratiform region (1910–1912). FL4b profiles again show  $T_b$ 's at 37 GHz and greater which are displaced downshear 20 km from the radar measured rain areas (Figs. 12a and 12b). This is not surprising in view of the apparent lack of ice above the rain layer (FL4b at about 1913 in Fig. 17).

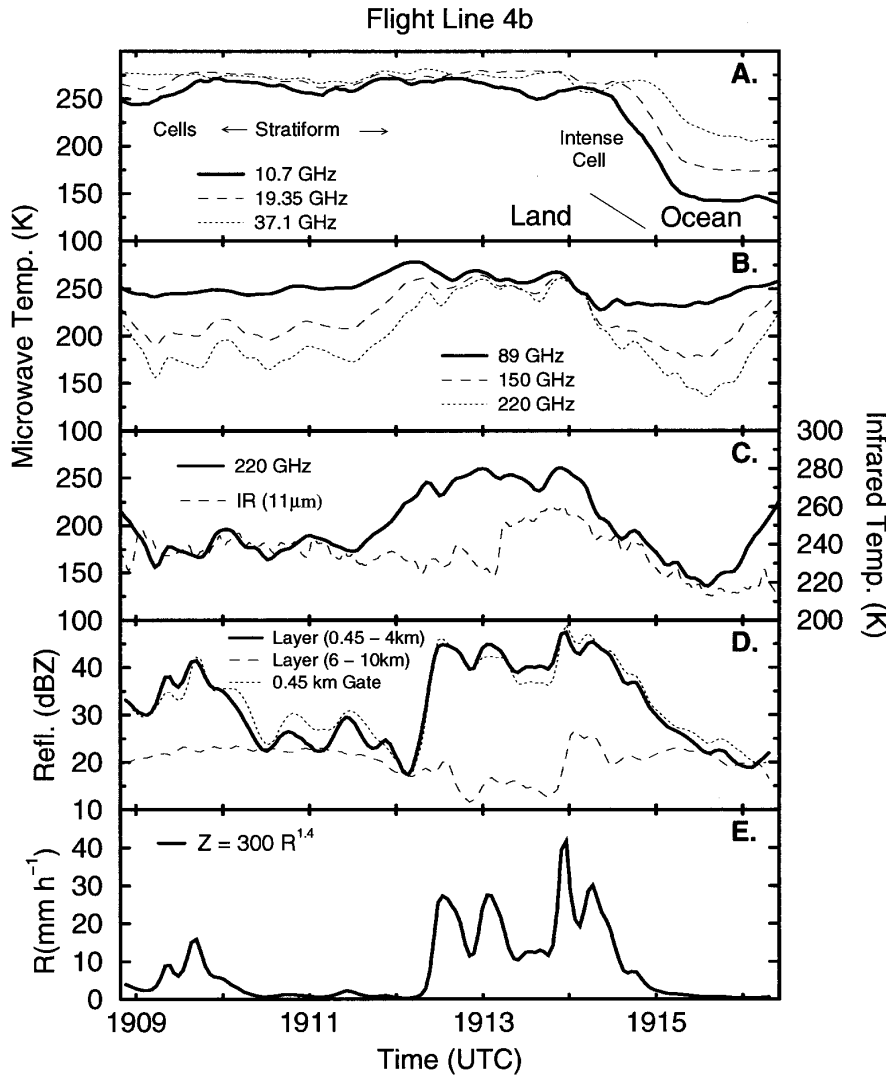


FIG. 12. Profiles of radiometric and radar data for flight line FL4b along nadir (horizontal dashed line in Fig. 7); otherwise similar to Fig. 8.

The general lack of correlation between the microwave  $T_b$ 's and the rainfall rates over land is demonstrated by Fig. 13, which presents a  $T_b$ -rainfall rate plot for the FL4a and FL4b land-based flight lines. Over land, the surface emissivity is close to unity and often there is little contrast between the emission from rain at lower frequencies and the land background (e.g., Wilheit 1986). Unless the storms have significant ice to provide strong scattering, rain can also remain undetected at the higher frequencies. This is indeed the case in Fig. 13, where the  $T_b$ 's are nearly constant with rainfall rate. Note also the effect of the variable surface emission for the points at low rainfall rates. The scatter for low rainfall rates at all frequencies is 40–60 K. Many of these points have been correlated with a swampy area, which is part of the Everglades. Previous studies (Heysfield and Fulton 1992) have shown that during and after rainfall, increased soil moisture and/or standing water can produce significant lowering of the  $T_b$ 's, particularly if there is sparse vegetation. Except in situations where the rainfall rates are extremely high, brightness temperature depressions due to rain from land-based Florida thunderstorms can be lost in the highly variable background  $T_b$ 's.

## 6. Structure of the ice region from higher-frequency passive measurements

Determining properties of the ice region from the radiometric measurements is complicated by the known dependence of the ice-scattering mechanism on the details of the vertical distributions of ice microphysical properties (particle bulk densities, size distributions, shapes, etc.). Only very simple ice crystals (horizontally oriented hexagonal plates, columns, and needles) have been modeled with radiative transfer calculations (Wu and Weinman 1984; Evans and Vivekanandan 1990); actual clouds are much more complex, particularly in convective regions. Their results show that ice particle shape is important for radiometry at high frequencies. Also, supercooled water, which often occurs in thunderstorms, can complicate the retrieval of properties from the ice phase region. The purpose here is to study the general characteristics of the ice layer by examining the relations between the various  $\Delta T_b$ 's between 37 and 220 GHz to determine whether they can be related to characteristics of the ice layer obtained from the EDOP reflectivity measurements.

The bulk properties of the ice and mixed phase region of thunderstorms have been examined by Vivekanandan et al. (1991) using radiative transfer calculations to simulate spaceborne  $T_b$ 's for layers of precipitation-sized hydrometeors of variable bulk density and ice water content. Bulk properties are simpler to examine because of the difficulties in specifying the ice particle characteristics necessary for modeling the ice region. Results from Vivekanandan et al. show that the integrated ice path (IP) can be estimated from the tem-

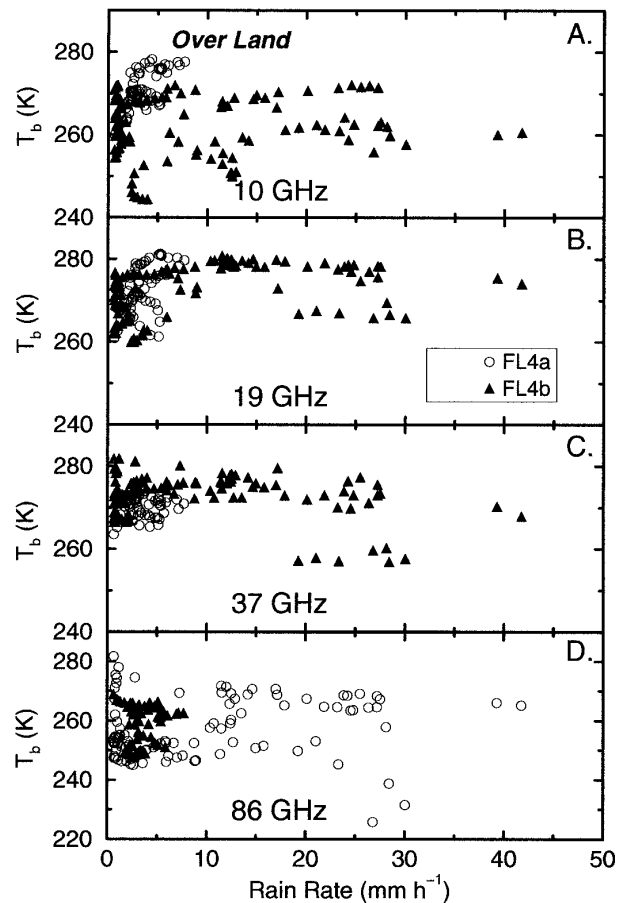


FIG. 13. Similar to Fig. 10 except for land-based flight lines FL4a and FL4b.

perature difference  $\Delta T_b(37-85) = T_b(37 \text{ GHz}) - T_b(85 \text{ GHz})$ . The parameter  $IP \equiv \int IWC(z) dz$ , where  $IWC$  is the ice water content and the integration is taken over the depth of the ice layer. The relation between  $IP$  and  $\Delta T_b(37-85)$  depends on various factors including the bulk ice density and the presence of supercooled water and the underlying rain layer. According to Vivekanandan et al., the 37–85-GHz difference is not strongly affected by the underlying rain region since the 37- and 85-GHz channels saturate at low rainfall rates. Not only are we interested in exploring the  $\Delta T_b(37-85)$  relation to  $IP$  suggested by Vivekanandan et al. (1991), but also the apparent sensitivity of the frequencies above 85 GHz to ice in the anvil regions of thunderstorms. Also from a satellite retrieval perspective, the higher frequencies are of intrinsic interest since they provide somewhat better resolution (i.e., the footprint scales in inverse proportion to frequency). As the frequency is increased, the Mie scattering becomes more effective for smaller ice particles according to the well-known size parameter  $\pi D/\lambda > 1$ , where  $D$  is particle diameter and  $\lambda$  is wavelength. Is there any evi-

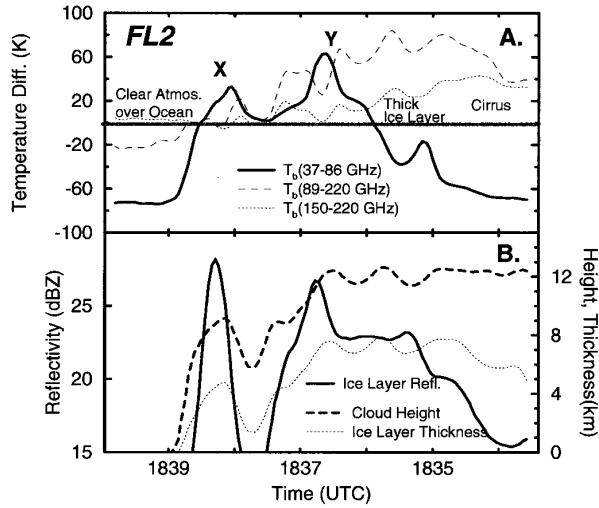


FIG. 14. Flight line FL2 profiles emphasizing ice-layer characteristics. Shown in (a) are microwave brightness temperature differences  $\Delta T_b$  and (b) ice-layer characteristics from EDOP observations. Thick horizontal bar in (a) shows  $\Delta T_b = 0$  K reference.

dence of size dependence on the higher-frequency microwave measurements and can they alone provide useful information about cloud classification?

Figures 14–17 show several microwave  $\Delta T_b$ 's (37–86 GHz, 89–220 GHz, and 150–220 GHz), ice-layer thickness, mean ice-layer reflectivity, and cloud height for each flight line as a function of time; the  $\Delta T_b$  (89–150 GHz) curves, which fall between  $\Delta T_b$  (89–220 GHz) and  $\Delta T_b$  (37–86 GHz), are not presented for clarity of the figure. These sections cover the same time periods as the profiles plotted previously in Figs. 8, 9, 11, and 12. The  $\Delta T_b$ 's were obtained from the interpolated combined fields described previously, and the

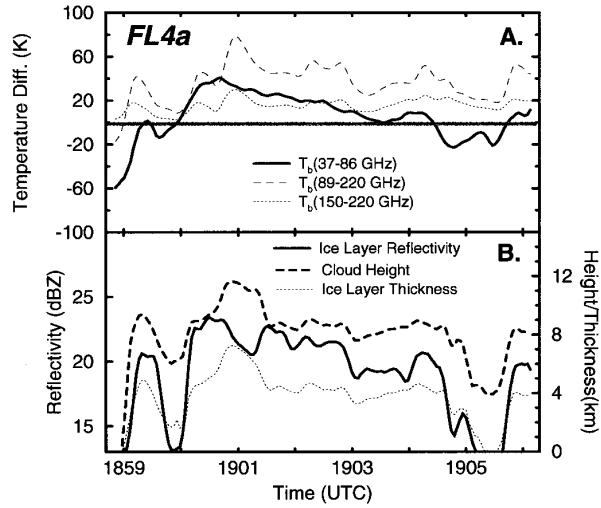


FIG. 16. Same as Fig. 14 except for flight line FL4a.

cloud heights were taken from the highest radar range gates with data above the noise threshold. Note that the AMPR 85.5-GHz channel (indicated by 86 GHz) is used in the 37–86-GHz difference in order to mitigate errors resulting from interpolation of MIR and AMPR  $\Delta T_b$ 's to common time intervals. The ice-layer thicknesses obtained from the EDOP data are calculated from the number of 150-m range gates between the ice-layer base (i.e., freezing level at 4.6 km) and cloud top based on reflectivity. This thickness can be less than the difference between cloud top and the freezing level (e.g., see Fig. 3 for FL2 at 1836), and it does not account for the possibility that supercooled water may exist above the freezing level.

General characteristics from the four flight lines in Figs. 14–17 have been summarized in Table 1. The

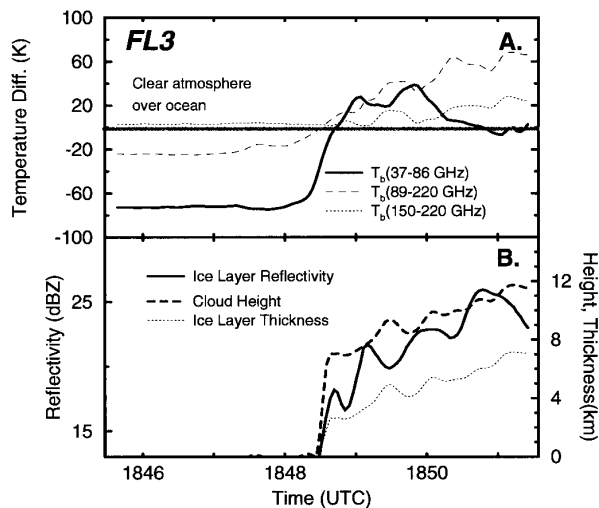


FIG. 15. Same as Fig. 14 except for flight line FL3.

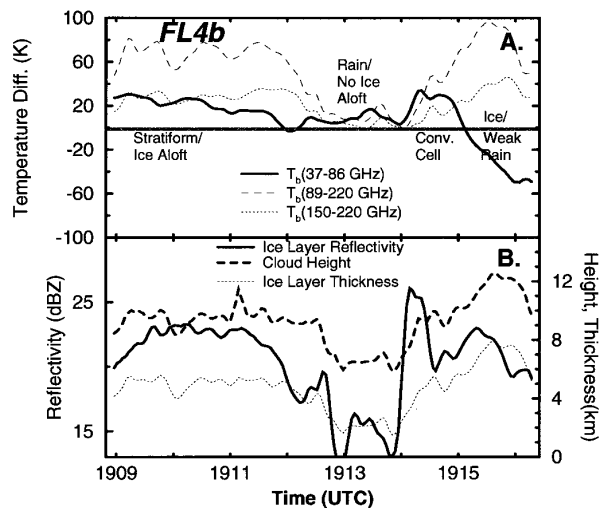


FIG. 17. Same as Fig. 14 except for flight line FL4b.

TABLE 1. Typical magnitudes of  $\Delta T_b$  under various conditions.

	$\Delta T_b$ (37–86 GHz)	$\Delta T_b$ (89–220 GHz)	$\Delta T_b$ (150–220 GHz)
Convective core	40 K	20 K	~0 K
Thin anvil ice layer	-70 K	40 K	40 K
Rain (no ice layer)	~0 K	~0 K	~0 K
Clear ocean background	-70 K	-20 K	~0 K

table suggests that scattering-based radiometric observations from 37 to 220 GHz can provide useful information on distinguishing thin ice layers from ice in convective cores, and from rain layers without overlying ice. The plots are summarized in general terms in the following.

*a. Convective regions with a deep ice layer and underlying rain*

The  $\Delta T_b$  (37–86 GHz)'s have the largest positive values associated with convective cores, which have high reflectivities near the surface and aloft. The  $\Delta T_b$  (37–86) are generally correlated with the higher reflectivity cores present above the freezing level, particularly for storm Y during FL2 (Fig. 14 at 1836:30), and for convective storms during FL4a (Fig. 16 at 1901) and FL4b (Fig. 17 at 1915:30). These values range from a peak of 80 K (storm Y during FL2) to more typical values of 40 K in convective cells during the other flight lines. The general range of values here are consistent with those calculated by Vivekanandan et al. (1991). However, storm X and Y points are on the high end of the Vivekanandan et al. curves (Figs. 1 and 2 in their paper). Interestingly, the  $\Delta T_b$  (37–86)  $> 0$  are well correlated with ice-layer reflectivities greater than about 23 dBZ, and there is no obvious correlation with ice-layer thickness.

The higher-frequency measurements show that  $\Delta T_b$  (89–220 GHz) is large in both the convective and stratiform regions, and  $\Delta T_b$  (150–220 GHz) parallels the  $\Delta T_b$  (89–220 GHz)'s, but with lower magnitudes. The positive values indicate that the  $T_b$  (220 GHz)'s are more sensitive to scattering from the ice than the  $T_b$  (86 GHz)'s. Comparison of the ice-layer thicknesses and reflectivities with the  $\Delta T_b$ 's indicate that they must be greater than about 3 km and 15 dBZ, respectively, for the  $\Delta T_b$ 's to be much larger than zero as present in the stratiform and convective regions.

*b. Thin anvil ice layers without underlying rain*

The  $\Delta T_b$  (89–220 GHz) and  $\Delta T_b$  (150–220 GHz) are both greater than zero and of similar magnitude since only the  $T_b$  (220 GHz) is responding to the ice layer, and the layer is fairly transparent to the 86- and 150-GHz channels. This is evident for FL2 after 1835 (Fig. 14) where the elevated cirrus layer is greater than 5 km thick and the reflectivities are about 15 dBZ; for con-

vective regions in 1) above, ice-layer thicknesses were thinner (~3 km thick). Also note that  $\Delta T_b$  (37–86 GHz) is much less than zero since neither the 37- or 86-GHz frequencies detect the ice layer and the 37-GHz emission provides a lower  $T_b$  than at 86 GHz. This clearly shows the sensitivity of the 220-GHz  $T_b$ 's to a thunderstorm-generated cirrus layer and possibly provides a method for determining bulk properties of cirrus layers. Note that the ice particles in this layer are likely to be larger than typical for cirrus clouds since the reflectivities here are greater than for cirrus. Atlas et al. (1995) have shown that typical cirrus reflectivities range from roughly -50 dBZ up to +10 dBZ. Cirrus ice particles have a wide range of mean sizes (i.e., 25–1000  $\mu\text{m}$ ). For the 15-dBZ reflectivities observed here, plots in Atlas et al. paper indicate high IWC are present and that mean ice particle dimensions are likely to be on the high end for cirrus clouds (i.e., 500–1000  $\mu\text{m}$ ).

*c. Rain region without a significant ice layer aloft*

In regions without a deep ice layer overlying the rain below the freezing level, all the  $\Delta T_b$ 's approach 0 K (Fig. 17 at 1913–1914). Lowering of the  $T_b$ 's by ice scattering appears to require reflectivities greater than about 15 dBZ and ice-layer thicknesses greater than a few kilometers. Note that none of the microwave  $T_b$ 's in Fig. 12 indicate with any certainty the presence of rain or ice over the land background. The Table 1 entries indicate that a rain layer (over land in this case) without a few-kilometer-thick ice layer aloft may be easily identifiable in a qualitative sense from other types of precipitation.

*d. Ocean background without clouds*

The  $\Delta T_b$  (37–86 GHz) and  $\Delta T_b$  (89–220 GHz) are much less than zero because the attenuation coefficient for water vapor increases with increasing frequency (except for water vapor windows such as at 183 GHz) (Waters 1976). This is apparent for FL2 between 1839 and 1840 (Fig. 14), FL3 before 1848 (Fig. 15), FL4a before 1859 (Fig. 16), and FL4b after 1915 (Fig. 17). Also note the  $\Delta T_b$  (150–220 GHz) is slightly larger than 0 K in these regions because of the greater water vapor absorption at 220 GHz (and hence lower  $T_b$ ) than at 150 GHz; these channels saturate as a result of water vapor absorption well above the surface.

The  $\Delta T_b$  observations above suggest a correlation with the ice-layer reflectivities and the ice-layer thicknesses, both of which are related to the IP. Examination of the relationship of the  $\Delta T_b$ 's to IP such as performed by Vivekanandan et al. (1991) is only possible in very crude terms here since the calculation of IP requires knowledge of the IWC. Rough estimates of IWC were made for the four flight line datasets presented in this paper using a  $Z$ -IWC relation. The  $Z$ -IWC relations can vary considerably with altitude, temperature, location, etc. (Atlas et al. 1995). Most of the  $Z$ -IWC relations in the literature are based on cirrus measurements and are not suitable for the larger convective and stratiform reflectivities as in the present study. An attempt was made to use  $Z$ -IWC relations for convective and stratiform situations based on Pre STORM in situ observations and other midlatitude in situ data.<sup>3</sup> These relations were used to calculate IP from the EDOP-derived ice-layer reflectivity. The plots of  $\Delta T_b$  versus IP are not presented here since they showed a high degree of scatter with a poor fit to a linear curve. The lack of a well-defined relationship between  $\Delta T_b$ 's and IP is partly due to the large uncertainty in the IWC estimates and the large differences in the vertical and horizontal ice structure during the different flight lines. Also, the presence of supercooled water above the freezing level would have the effect of masking the scattering signal, and thereby warming the  $T_b$ 's to produce a smaller temperature difference. Nevertheless, there appears to be some useful qualitative and possibly quantitative information on the relative amounts of ice present in the convective cores. There have been proposals to place high-frequency microwave radiometers on future geostationary satellites. These results suggest that qualitative classification of the precipitating and nonprecipitating clouds can be made using scattering-based frequencies of 86 GHz and above.

## 7. Summary and conclusions

This paper provides an analysis of a unique remote sensing dataset from the NASA ER-2 high-altitude aircraft overflying Florida thunderstorms on 5 October 1993 during CAMEX. For the first time during CAMEX, downlooking radar reflectivity measurements were obtained from the new ER-2 Doppler radar system (EDOP). The availability of EDOP data with simultaneous ER-2 high-frequency microwave radiometric measurements greatly enhanced the interpretation of the microwave and IR remote sensing measurements of the thunderstorms.

The analysis focused on two types of convection: a small group of thunderstorms over the Florida Straits and sea-breeze-initiated convection along the Florida

Atlantic coast. Both types of thunderstorms studied showed reflectivities consistent with warm rain coalescence processes, although the land-based convection had higher reflectivities several kilometers above the freezing level. The land-based radar reflectivities suggested the presence of either supercooled water or larger ice particles, possibly water coated, above the freezing level in these cells. However, much of the convective and stratiform regions lacked high reflectivities above the freezing level, consistent with reflectivity structures found in tropical oceanic cells (e.g., Szoke et al. 1986; Jorgensen et al. 1989), which are characterized by weak updrafts, rapidly glaciating cells, and smaller particles aloft (less than a few millimeters).

The relation of the microwave and IR brightness temperatures were examined in detail and related to the vertical structure of the precipitation region determined from the EDOP radar observations. The rain cores observed over ocean by EDOP were well correlated with elevated microwave brightness temperatures from the AMPR 10.7-GHz channel. The microwave  $T_b$ 's at frequencies above 37 GHz, which are scattering based, were not well correlated with surface rainfall rate. As noted in previous studies, the ice-scattering regions evident in the microwave  $T_b$ 's above 37 GHz, were displaced significantly downshear of the convective region due to advection by upper-level winds. The IR  $T_b$ 's corresponded well with the radar-observed thunderstorm ice regions, which were poorly correlated with surface rainfall in the cases studied here. The observations clearly show that the interpretation of the microwave  $T_b$ 's depend strongly on vertical wind shear. Rain retrieval algorithms based on 86-GHz measurements alone would be in error for instantaneous looks at clouds because they rely on the indirect association of ice aloft with rainfall at the surface; these methods incorporate significant averaging over space and time and are generally used for monthly rain estimates.

The microwave and radar observations over land were very interesting in that they clearly showed the difficulty in detecting rain using emission-sensitive microwave channels. This well-known problem was previously difficult to illustrate using aircraft radiometric observations without simultaneous radar observations. On the land-based flight lines, the higher-frequency ice-scattering signal (86 GHz) was only weakly correlated with low-level reflectivity and rainfall rate because the ice region was displaced downwind from the convective rain region. The scattering-sensitive, higher microwave channels, which have been considered to be the main method for spaceborne rain estimation over land, would not agree well with coincident, instantaneous radar estimates due to the ambiguities that can result from the vertical wind shear. Also, the effect of storm evolution on the microwave and IR  $T_b$ 's is important as shown in previous studies such as Fulton and Heymsfield (1991). It was not possible in the present study to examine storm evolution due to limitations of

<sup>3</sup> Relations are based on discussions with Dr. A. Heymsfield, National Center for Atmospheric Research.

the data. The precipitation radar (PR) employed in TRMM will greatly help with difficulties associated with land-based precipitation estimation using radiometers.

The rainfall rates calculated from EDOP reflectivity measurements and simultaneous microwave brightness temperature observations have been compared to radiative transfer model calculations of  $T_b$ 's using a family of cloud model derived vertical profiles. Single-frequency brightness temperature calculations based upon a "TOGA COARE" cloud model simulation agreed fairly well with the observed radar rainfall rate- $T_b$  data points, while brightness temperatures computed from a "GATE" simulation were consistently lower than those observed. The difference between the observed and computed brightness temperatures in the latter case is attributed to greater rain cell vertical development than in the GATE simulation, resulting in more radiative scattering by precipitation-sized ice. Multifrequency rain and vertical structure retrievals have been performed by Kummerow et al. (1995) and Olson et al. (1995) using some of the EDOP and AMPR data here.

The radar and radiometer datasets presented in this paper provided the opportunity to examine the sensitivity of higher-frequency passive microwave measurements (89–220 GHz) to the amount of ice present. The analyzed brightness temperature differences  $\Delta T_b$ 's (37–86 GHz, 89–220 GHz, and 150–220 GHz) indicated some correlation with the ice-layer reflectivities and thicknesses. These temperature differences provided useful information for distinguishing thin ice layers from ice in convective cores, and from rain layers without overlying ice. From the data presented, it was found that reflectivities and ice-layer thicknesses must be greater than about 15 dBZ and a few kilometers, respectively, to produce significant ice scattering at frequencies above 90 GHz. More radar and radiometer datasets are now available to examine the generality of the above findings. Possibly in the future, multifrequency microwave retrievals can be applied to the predominantly scattering-based channels (above 37 GHz) to provide quantitative information regarding the ice region. However, the ability of the retrievals to perform well utilizing the higher-frequency data may depend on the correct specification of additional ice microphysical information required in supporting radiative calculations.

Multifrequency radiometer measurements alone do not have adequate information to obtain vertical profiles, and therefore profiling algorithms rely on cloud models to provide microphysical information. Cloud models, in turn, require validation against actual observations, particularly microphysical information. These datasets can only be obtained through comprehensive field campaigns such as TOGA COARE and future campaigns planned for the TRMM validation. More recent experiments have been conducted with the

full-up EDOP system, including Doppler and polarization measurements along with other radiometers and cloud electrification instruments. These datasets will contribute to a better understanding of the relationships between cloud microphysical structure, top-of-the-atmosphere microwave and IR brightness temperatures, and cloud electrification. The EDOP on future flights will possibly be able to qualitatively differentiate rain, ice, and perhaps hail using linear depolarization measurements. This will be useful in determining whether supercooled water is present above the freezing level in convective cells. However, the most crucial observations for future campaigns are detailed in situ microphysical observations throughout the cloud depth, particularly in the ice region.

*Acknowledgments.* The datasets presented in this paper required considerable effort in both acquisition and processing. First, the authors are appreciative of the large engineering effort by the Goddard Microwave Sensors Branch headed by L. Thompson in preparing EDOP for its first measurements during CAMEX. Also, S. Nicholson under a NASA Global Science Fellowship at the University of Kansas, participated extensively in the development of the EDOP data system. Acknowledgment is also given to the efforts of the other instrument teams involved in CAMEX. The calibrated AMPR, MIR, and MAMS data have been provided by R. Hood of Marshall Space Flight Center (MSFC), J. Wang of GSFC, and J. Meyers of Ames Research Center, respectively. Radar composites from the Florida WSR-88D radars were provided by V. Griffin of MSFC. P. Keehn and E. Nelkin of SSAI are appreciated for helping with GOES and radar data in McIDAS format. Paul Hubanks of Research Data Systems, Inc., provided software to process the MAS data. Finally, there have been helpful discussions about the work with J. Weinman, C. Kummerow, J. Wang, B. Ferrier, and R. Adler of GSFC. B. Ferrier, in particular, gave helpful insights on tropical microphysical observations and modeling results. The funding for this work has been provided by Dr. R. Kakar of NASA HQ under the Mission to Planet Earth.

#### APPENDIX

##### EDOP Characteristics

Frequency	9.72 GHz
Wavelength	3.07 cm
Peak power (split between two antennas)	20 kW
Pulse length	0.25, 1.0 $\mu$ s
PRF	2200, 4400
Antenna diameter	0.76 m
Antenna beamwidth	2.9°
Receiver dynamic range with gain control	110 dB
Number of Doppler channels	2

Number of log reflectivity channels	3
Integration interval	0.25, 0.5, 1 s
Nadir beam	
Transmit polarization	Vertical
Received polarization	Copolarized
Forward beam	
Transmit polarization	Vertical
Received polarization	Copolarization and Cross-polarization

## REFERENCES

- Adler, R. F., and A. J. Negri, 1988: A satellite infrared technique to estimate tropical convective and stratiform rainfall. *J. Appl. Meteor.*, **27**, 280–296.
- , R. Mack, N. Prasad, H. Yeh, and I. Hakkarinen, 1990: Aircraft microwave observations and simulation of deep convection from 18 to 183 GHz. Part I: Observations. *J. Atmos. Oceanic Technol.*, **7**, 377–391.
- , H.-Y. M. Yeh, N. Prasad, W.-K. Tao, and J. Simpson, 1991: Microwave simulations of a tropical rainfall system with a three-dimensional cloud model. *J. Appl. Meteor.*, **30**, 924–953.
- , A. J. Negri, P. R. Keehn, and I. M. Hakkarinen, 1993: Estimation of monthly rainfall over Japan and surrounding waters from a combination of low orbit microwave and geosynchronous IR data. *J. Appl. Meteor.*, **32**, 335–356.
- Atlas, D., S. Y. Matrosov, A. J. Heymsfield, M. D. Chou, and D. B. Wolff, 1995: Radar and radiation properties of ice clouds. *J. Appl. Meteor.*, **34**, 2329–2345.
- Bringi, V. N., I. J. Caylor, J. Turk, and L. Liu, 1993: Microphysical and electrical evolution of a convective storm using multiparameter radar and aircraft data during CaPE. Preprints, *26th Conf. on Radar Meteorology*, Norman, OK, Amer. Meteor. Soc., 312–314.
- Caylor, I. J., G. M. Heymsfield, S. Bidwell, and S. Ameen, 1994: NASA ER-2 Doppler radar reflectivity calibration for the CAMEX project. NASA Tech. Memo. 104611, 15 pp. [Available from NASA Center for AeroSpace Information, 800 Elkridge Landing Road, Linthicum Heights, MD 21090-2934.]
- Durden, S. L., E. Im, F. K. Li, W. Ricketts, A. Tanner, and W. Wilson, 1994: ARMAR: An airborne rain-mapping radar. *J. Atmos. Oceanic Technol.*, **11**, 727–737.
- Evans, K. F., and J. Vivekanandan, 1990: Multiparameter radar and microwave radiative transfer modeling of nonspherical atmospheric ice particles. *IEEE Trans. Geosci. Remote Sens.*, **28**, 423–437.
- Fulton, R., and G. M. Heymsfield, 1991: Microphysical and radiative characteristics of convective clouds during COHMEX. *J. Appl. Meteor.*, **30**, 98–116.
- Gasiewski, A. J., 1992: Numerical sensitivity analysis of passive EHF and SMMW channels to tropospheric clouds, water vapor, and precipitation. *IEEE Trans. Geosci. Remote Sens.*, **30**, 859–870.
- Griffin, V. L., A. R. Guillory, M. Susko, and J. E. Arnold, 1994: Operations summary for the Convection and Moisture Experiment (CAMEX). NASA Tech. Memo. TM-108445, 180 pp.
- Gumley, L. E., P. A. Hubanks, and E. J. Masuoka, 1994: MODIS Airborne Simulator Level 1B data user's guide. NASA Tech. Memo. 104594, Vol. 3, 37 pp.
- Hakkarinen, I. M., and R. F. Adler, 1988: Observations of precipitation convective systems at 92 and 183 GHz: Aircraft results. *Meteor. Atmos. Phys.*, **38**, 164–182.
- Heymsfield, G. M., and R. Fulton, 1988: Comparison of high-altitude remote aircraft measurements with the radar structure of an Oklahoma thunderstorm: Implications for precipitation estimation from space. *Mon. Wea. Rev.*, **116**, 1157–1174.
- , and —, 1992: Modulation of SSM/I microwave soil radiances by rainfall. *Remote Sens. Environ.*, **39**, 187–202.
- , W. Bonczyk, S. Bidwell, D. Vandemark, S. Ameen, S. Nicholson, and L. Miller, 1993: Status of the NASA/EDOP airborne radar system. Preprints, *26th Conf. on Radar Meteorology*, Norman, OK, Amer. Meteor. Soc., 374–375.
- Houze, R. A., Jr., 1977: Structure and dynamics of a tropical squall line-system. *Mon. Wea. Rev.*, **105**, 1540–1567.
- Jedlovec, G. J., K. B. Batson, R. J. Atkinson, C. C. Moeller, W. P. Menzel, and M. W. James, 1989: Improved capabilities of the Multispectral Atmospheric Mapping Sensor (MAMS). NASA Tech. Memo. 100352, 71 pp.
- Jorgensen, D. P., and M. A. LeMone, 1989: Vertical velocity characteristics of oceanic convection. *J. Atmos. Sci.*, **46**, 621–640.
- Kakar, R., Ed., 1993: Mission summary reports. NASA COARE, 236 pp. [Available from NASA Headquarters, Code YS, Washington, DC 20546-0010.]
- Kummerow, C., and L. Giglio, 1994: A passive microwave technique for estimating the vertical structure of rainfall from space. Part I: Algorithm description. *J. Appl. Meteor.*, **33**, 3–18.
- , R. A. Mack, and I. M. Hakkarinen, 1989: A self-consistency approach to improve microwave rainfall estimation from space. *J. Appl. Meteor.*, **28**, 869–884.
- , W. S. Olson, and L. Giglio, 1996: A simplified scheme for obtaining precipitation and vertical hydrometer profiles from passive microwave sensors. *IEEE Trans. Geosci. Remote Sens.*, in press.
- McGaughey, G., E. J. Zipser, R. W. Spencer, and R. E. Hood, 1996: High-resolution passive microwave observations of convective systems over the tropical Pacific Ocean. *J. Appl. Meteor.*, in press.
- Meneghini, R., and D. Atlas, 1986: Simultaneous ocean cross section and rainfall measurements from space with a nadir-looking radar. *J. Atmos. Oceanic Technol.*, **3**, 400–413.
- Olson, W. S., 1989: Physical retrieval of rainfall rates over the ocean by multispectral microwave radiometry: Application to tropical cyclones. *J. Geophys. Res.*, **94**, 2267–2280.
- , C. D. Kummerow, G. M. Heymsfield, and L. Giglio, 1996: A method for combined passive-active microwave retrievals of cloud and precipitation profiles. *J. Appl. Meteor.*, **35**, 1763–1789.
- Racette, P., R. F. Adler, A. J. Gasiewski, D. M. Jackson, J. R. Wang, and D. S. Zacharias, 1996: An airborne millimeter-wave imaging radiometer for cloud, precipitation, and atmospheric water vapor studies. *J. Atmos. Oceanic Technol.*, **13**, 610–619.
- Simpson, J. Ed., Report of the science steering group for a Tropical Rain Measurement System (TRMM). NASA, 94 pp. [Available from TRMM Office Code 9101.1, GSFC, Greenbelt, MD 20771.]
- , R. F. Adler, and G. R. North, 1988: A proposed Tropical Rainfall Measuring Mission (TRMM) satellite. *Bull. Amer. Meteor. Soc.*, **69**, 278–295.
- Smith, E. A., X. Xiang, A. Mugnai, R. E. Hood, and R. W. Spencer, 1994: Behavior of an inversion-based precipitation retrieval algorithm with high-resolution AMPR measurements including a low-frequency 10.7-GHz channel. *J. Atmos. Oceanic Technol.*, **11**, 858–873.
- Spencer, R. W., 1984: Satellite passive microwave rainfall rate measurement over croplands during spring, summer, and fall. *J. Climate Appl. Meteor.*, **23**, 1555–1556.
- , 1986: A satellite 37 GHz scattering-based method for measuring oceanic rainfall rates. *J. Climate Appl. Meteor.*, **25**, 754–766.
- , H. M. Goodman, and R. E. Hood, 1989: Precipitation retrieval over land and ocean with SSM/I: Identification and characteristics of the scattering signal. *J. Atmos. Oceanic Technol.*, **6**, 254–273.
- , and Coauthors, 1994: High-resolution imaging of rain systems with the Advanced Microwave Precipitation Radiometer. *J. Atmos. Oceanic Technol.*, **11**, 849–857.
- Szoke, E. J., E. J. Zipser, and D. P. Jorgensen, 1986: A radar study of convective cells in mesoscale systems in GATE. Part I: Ver-

- tical profile statistics and comparison with hurricanes. *J. Atmos. Sci.*, **43**, 182–197.
- Tao, W.-K., and J. Simpson, 1989: Modeling study of a tropical squall-type convective line. *J. Atmos. Sci.*, **46**, 177–202.
- Vivekanandan, J., J. Turk, G. L. Stephens, and V. N. Bringi, 1989: Microwave radiative transfer studies using combined multiparameter radar and radiometer measurements during COHMEX. *J. Appl. Meteor.*, **28**, 561–585.
- , —, and V. N. Bringi, 1991: Ice water path estimation and characterization using passive microwave radiometry. *J. Appl. Meteor.*, **30**, 1407–1421.
- , —, and —, 1993: Comparisons of precipitation measurements by the Advanced Microwave Precipitation Radiometer and multiparameter radar. *IEEE Trans. Geosci. Remote Sens.*, **31**, 860–870.
- Yuter, S. E., and R. A. Houze Jr., 1995: Three-dimensional kinematic and microphysical evolution of Florida cumulonimbus. Part I: Spatial distribution of updrafts, downdrafts, and precipitation. *Mon. Wea. Rev.*, **123**, 1921–1943.
- Wang, J. R., R. Meneghini, H. Kumagai, T. T. Wilheit Jr., W. C. Bonyk, R. Racette, J. R. Tesmer, and B. Maves, 1994: Airborne active and passive microwave observations of Typhoon Flo. *IEEE Trans. Geosci. Remote Sens.*, **32**, 231–242.
- Waters, J. W., 1976: Absorption and emission of microwave radiation by atmospheric gases. *Methods of Experimental Physics: Astrophysics*, Vol. 12, N. Carleton, Ed., Academic Press, 309 pp.
- Weinman, J. A., and R. Davies, 1978: Thermal microwave radiances from horizontally finite clouds of hydrometeors. *J. Geophys. Res.*, **83**, 3099–3107.
- Weisman, M. L., and J. B. Klemp, 1982: The dependence of numerically simulated convective storms on vertical wind shear and buoyancy. *Mon. Wea. Rev.*, **110**, 504–520.
- Wilheit, T. T., 1986: Some comments on passive microwave measurement of rain. *Bull. Amer. Meteor. Soc.*, **67**, 1226–1232.
- , A. T. C. Chang, M. S. V. Rao, E. B. Rodgers, and J. S. Theon, 1977: A satellite technique for quantitatively mapping rainfall rates over the ocean. *J. Appl. Meteor.*, **16**, 551–560.
- Woodley, W., and A. Herndon, 1970: A raingage evaluation of the Miami reflectivity–rainfall rate relation. *J. Appl. Meteor.*, **9**, 258–264.
- Wu, R., and J. A. Weinman, 1984: Microwave radiances from precipitating clouds containing aspherical ice, combined phase, and liquid hydrometeors. *J. Geophys. Res.*, **89**, 7170–7178.